Article

Geometrical interpretation of the hydrogen atom hyperfine structure

Barry R. Clarke

Oxford, UK; *aleteller@barryispuzzled.com*

Abstract

A phenomenological geometrical model is presented for the hyperfine structure of hydrogenic systems. The approach extends a previously published fine-structure analysis to hyperfine splittings by introducing a compact set of empirically constrained geometric corrections. Unlike conventional quantum electrodynamic treatments which reference the Lamb shift to the hyperfine centroid, the present framework targets the hyperfine midpoint, corresponding to a substantially larger reference interval. Despite this difference in reference scale, agreement with experimental hyperfine and Lamb-shift-related data at the 0.01 MHz level is obtained across multiple hydrogen states. The model is further extended to deuterium, tritium, ^{3}He$^+$, and ^{7}Li^{2+}, revealing systematic cross-nuclear behaviour and a universal scaling relation involving nuclear mass number and charge. The calculations employ a simplified geometric scheme that does not rely on perturbative quantum electrodynamics but is intended as a complementary phenomenological description. Possible physical interpretations in terms of structured internal dynamics are discussed, together with limitations and directions for further development.

Keywords: *photonics; SAM; OAM; photonic; toroidal; vortex; hydrogen; atom; hyperfine; structure*

1. Introduction

1.1. Preliminary

Atomic hyperfine structure is conventionally described within quantum electrodynamics (QED) using perturbative expansions that incorporate relativistic, radiative, and nuclear effects. These calculations have achieved remarkable quantitative success but often involve substantial computational complexity and limited geometrical transparency. This has motivated the exploration of alternative representations that aim to capture observed regularities using reduced or explicitly structured formalisms [1–4].

The present work extends a previously published phenomenological geometrical framework, originally applied to fine structure phenomena, to the hyperfine structure of hydrogenic systems [4]. Within this framework, atomic energy shifts are represented using structured internal degrees of freedom that admit a geometrical interpretation. The model is not derived from perturbative QED, nor is it intended to replace it; rather, it offers a complementary phenomenological description in which mass, electric potential, magnetic fields, and electromagnetic induction are represented within geometric and rotational structure.

Academic Editor(s): Name

Received: date
Revised: date
Accepted: date
Published: date

https://doi.org/10.3390/xxxxx

A distinctive feature of the model is its focus on the hyperfine mid-point rather than the hyperfine centroid traditionally used in Lamb-shift calculations. This choice leads to a substantially greater reference frequency interval but allows the hyperfine splitting to be interpreted in terms of geometric field coupling between electronic and nuclear rotational modes. This newly-defined Lamb shift requires two empirically consistent corrections to the fine structure formula: a relative-to-proton speed adjustment, and a magnetic potential adjustment. Within the PTV framework, the magnetic potential adjustment is not treated as a static interaction evaluated at the bound-state radius, but as the accumulated effect of the proton's magnetic momentum field acting on the electron Sp-2 circuit as the electron is transported , within the model, from infinity to the bound-state separation. This interpretation parallels the cumulative Sp-3 interaction associated with bound-state formation.

The corrections employ four adjustable parameters, each associated with a specific physical or geometrical role.

The parameters Γ and A — Eqs. (13) and (22) — participate in the relative-to-proton speed adjustment and magnetic potential adjustment, respectively, while B in Eq. (22) is suggestive of a magnetic dipole-dipole interaction for all hydrogen and deuterium states. A fourth parameter k from Table VII in Eq. (35) governs the hyperfine shift and varies across angular momentum states. The parameter constraints are as follows. The Γ and A are connected through a universal scaling law that holds for hydrogen deuterium, tritium, ^{3}He$^+$, and ^{7}Li^{2+} in Eq. (37), while $B = -3.000$ is consistent across all hydrogenic states examined (Tables II, V, XI, and XII). For $nS_{1/2}$ states, $k = 1$ corresponds to the absence of any hyperfine adjustment and reinforces the Sp-2 parallel field assumption for magnetic interactions. Deviations from this k value for other states may be interpreted geometrically in terms of reduced proton field coupling arising from increased electronic eccentricity.

These features substantially reduce parameter freedom and distinguish the model from unconstrained empirical fitting. With the laboratory creation of photonic toroidal vortex states [5], precision OAM experiments provide a suggestive analogy for the structured elements employed in the model.

1.2. History and background

Experiments on electron vortices in transmission electron microscopes have shown that electrons can occupy quantized orbital states with large orbital angular momentum (OAM), even in free space, without a confining potential or external field [6–8]. This disassociation of quantized angular momentum from an external potential motivates the exploration of alternative representations alongside models such as Darwin's relativistic derivation of the hydrogen fine structure from Dirac's equation [9–10]. By combining Sommerfeld's classical treatment [11,12] with recent optical OAM experiments [13], a Photonic Toroidal Vortex (PTV) phenomenological model has been proposed in which the electron structure is represented using a toroidal geometric structure [4]. When this representation is applied in the presence of a corresponding proton structure, charge effects occur and fine-structure energies can be reproduced with high accuracy [4]. The present work introduces an effective representation of the observable electron rest mass in terms of a pure optical OAM, see Sec. 1.3.2. This geometrical model is then employed to estimate the Lamb shift and the hyperfine splitting of the hydrogen atom. An extension to deuterium, using the single-PTV hydrogen nucleus as an approximation, yields agreement at the level of 22 parts in one billion.

Interest in the hyperfine levels can be traced back to Lamb and Retherford's discovery that the $2S_{1/2}$ energy differs from the $2P_{1/2}$ by ~ 1000 MHz [14]. This violates Dirac's prediction. Quantum electrodynamics (QED) has produced successive corrections

[15–17], establishing the Lamb shift as the difference between the Sommerfeld–Dirac fine-structure energy and the experimental centroid of the hyperfine manifold. Here, the centroid arises from the mean of the hyperfine frequencies weighted according to transition amplitudes.

The standard relativistic and QED reference equations can be summarized as follows. Together they define the conventional hyperfine baseline against which the PTV modifications are applied. For an electron moving in the Coulomb field of a point nucleus, the frequency (MHz) is approximated by

$$\nu_{nk} = -\frac{2Z^2}{N(N+n+\gamma-k)}Ry \tag{1}$$

Here, Z is the nuclear charge, Ry is the Rydberg constant, n is the principal quantum number, $k = j + 1/2$ is the angular momentum quantum number, $\gamma = \sqrt{k^2 - (Z\alpha)^2}$, and $N = \sqrt{n^2 - 2(n-k)(k-\gamma)}$, see Table XVIII, Appendix A.[1]

The relativistic reduced mass correction (MHz) is

$$\Delta_{RM}\nu_{nk} = \frac{m_o}{m_o + m_o'}\left(1 - \frac{(Z\alpha)^2}{4n^2}\right)\nu_{nk} \tag{2}$$

where m_o and m_o' are the electron and proton rest masses, respectively.

For example, to calculate the Lamb shift for the $1S_{1/2}$ state of atomic hydrogen, we set $Z = 1$, $n = 1$, $k = 1$, and take the experimentally observed hyperfine centroid $\nu_{exp} = 3\,288\,086\,856.8$ MHz [18, Table 4]. The observed Lamb shift is then

$$\nu_{Lamb} = \nu_{11} - \Delta_{RM}\nu_{11} - \nu_{exp} \tag{3}$$

The first two terms on the right of Eq. (3) produce a magnitude of $3\,288\,095\,029.9$ MHz with the result that the hydrogen $1S_{1/2}$ state shifts by $\nu_{Lamb} = 8\,173.083\,5$ MHz.

The hyperfine splitting about the centroid, arising from magnetic dipole-dipole coupling between the electron and proton spins, is given in atomic units from Ref. [19, p.240], see Table XVIII, Appendix A:

$$\nu_{hf} = -\frac{10^{-6} g_p M \alpha^2}{2hn^3}\left(\frac{1}{1+M}\right)^3 \frac{F(F+1) - I(I+1) - j(j+1)}{j(j+1)(2l+1)} \tag{4}$$

where

$$M = \frac{m_o}{m_o'} \tag{5}$$

For example, for the ground state of hydrogen, the quantum numbers are nuclear spin $I = 1/2$, total quantum number $n = 1$, total electron angular momentum $j = 1/2$, and electron orbital angular momentum $l = 0$ which leaves

$$\nu_{hf} = -\frac{2(10^{-6}) g_p M \alpha^2}{3h}\left(\frac{1}{1+M}\right)^3 \left(F(F+1) - \frac{3}{2}\right) \tag{6}$$

Here, the total atomic angular momentum quantum number takes the values $F = 0, 1$. This gives $\nu_{hf}(F = 1) = -354.71$ MHz and $\nu_{hf}(F = 0) = 1064.13$ MHz. Figure 1 shows the shifts relative to the reduced mass adjusted fine-structure value, see Eq. (3).

---

[1] These equations have been modified from Johnson and Soff [17] to exhibit the units kg and MHz.

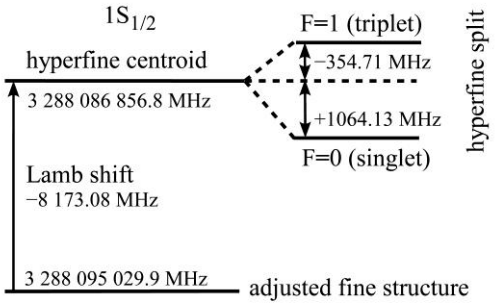

Figure 1. The magnitude of the ground state of hydrogen as calculated by QED [17]. The adjusted fine structure result with reduced mass is shown from Eqs. (1) and (2), the Lamb shift to the hyperfine centroid is obtained from Eq. (3), and the hyperfine splitting is calculated from Eq. (6) [19, p.240].

Full details of the QED Lamb shift calculation [17] and the hyperfine splitting [18, Sec. 3.1.1] are readily available.

1.3. *Assumptions of the PTV model*

In the specific realization adopted here, the structured internal degrees of freedom are represented by a Photonic Toroidal Vortex (PTV) model. The assumptions of the PTV model that are relevant to the present work are as follows [4, Fig. 3].

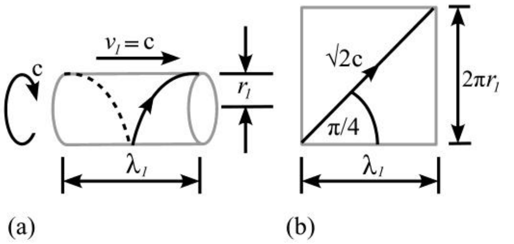

Figure 2. a A string following a helical path at speed $\sqrt{2}c$ and rake $\pi/4$ has both azimuthal and linear speed c. **b** Net of the helical string in **a** with wavelength $\lambda_1 = 2\pi r_1$.

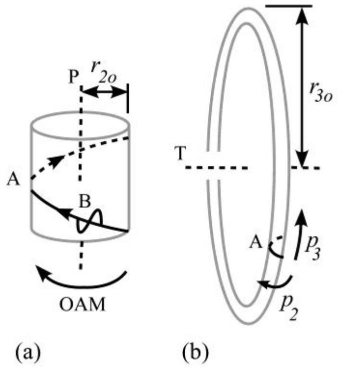

Figure 3. Construction of a PTV. **a** A helical string B from Fig. 2a circulates in a helical trajectory around an axis P as optical OAM on a notional tube A. This also has linear momentum parallel to axis P. **b** The notional tube A is given a curved trajectory about an axis T on a notional toroid. Here, P is the poloidal axis and T is the toroidal axis of the PTV. The magnetic and electric momenta are p_2 and p_3, respectively.

1.3.1. The helical string (Sp-1 rotation)

A string follows a helical trajectory at speed $\sqrt{2}c$ and rake $\pi/4$ so that it possesses both azimuthal and linear speed *c*. This constitutes a circular polarized ray or optical spin angular momentum (SAM) and is denoted as Sp-1, see Fig. 2.[2]

1.3.2. Optical OAM (Sp-2 rotation)

The string is then wrapped around a notional tube to form a Sp-2 rotation, see Fig. 3a. A closed trajectory constitutes the Sp-2 rest mass [4, Eq. (1)] and this is the electron rest mass m_o presented in Table XVIII or, on a smaller scale, the proton rest mass m'_o.

1.3.3. PTV construction (Sp-3 rotation)

The trajectory of the Sp-2 tube axis is subsequently curved into a toroidal path to form the complete Photonic Toroidal Vortex (PTV), characterized by poloidal rotation (Sp-2) and toroidal rotation (Sp-3), see Fig. 3b. The Sp-3 rotation constitutes an internal self-potential that plays the role of the external potential required in the Dirac–Sommerfeld scheme to produce results. The resulting bound-state geometry in the PTV model leads to the discrete fine-structure and, as shown in the present paper, also hyperfine-structure frequencies without invoking radiative-correction series. Without radiation absorption (unloaded case [4, Sec. 2]) the Sp-2 mass becomes relativistic with Sp-3 speed αc. This speed is reduced as oppositely-rotating radiation is absorbed (loaded case [4, Sec. 3]) and the toroids adopt higher energy levels. The 'higher' the energy level the smaller is the Sp-3 rotation frequency, [4, Sec. 3.1].[3]

The provision of Sp-3 speed v_3 to the electron rest mass m_o gives it a raised relativistic mass m_2 in the toroid which in ground state is given by [4, Eq. (10)] the following:[4]

$$m_2 = \frac{m_o}{(1-\alpha^2)^{1/2}} \tag{7}$$

Within the PTV framework, electric charge is associated with Sp-3 rotation, so that free electrons are treated as necessarily Sp-3 structured. Accordingly, within the PTV model, free electrons in metals, cathode rays, and beta rays are all Sp-3 rotations. This differs from the classical Bohr picture in which a free electron is taken to adopt a rotating orbit.

The poloidal and the toroidal momenta are orthogonal, giving rise to the magnetic (p_2) and electric (p_3) momentum components. These rotations continuously generate momentum fields, though their detailed propagation characteristics are represented by the parallel field approximation in Sec. 1.3.5.

1.3.4. PTV energy

The Sp-2 and Sp-3 energies of rotation are calculated from the following, respectively [4, Eqs. (4) and (48)]:

$$\varepsilon_2 = p_2 v_2, \quad \varepsilon_3 = p_3 v_3 \tag{8}$$

where momentum p and velocity v have adopted the rotation-type subscripts 2 and 3.

1.3.5. The momentum field

---

[2] This is the alternative helical string model suggested by Clarke [4, footnote 8] which appears to have greater possibilities than a non-rotating string advancing along its axis.

[3] The bound state distance from the nucleus also increases but the Sp-3 radius r_{3_o} remains constant.

[4] This is unlikely to be detected in changing magnetic fields which only affect the rest mass as pure Sp-2 rotation.

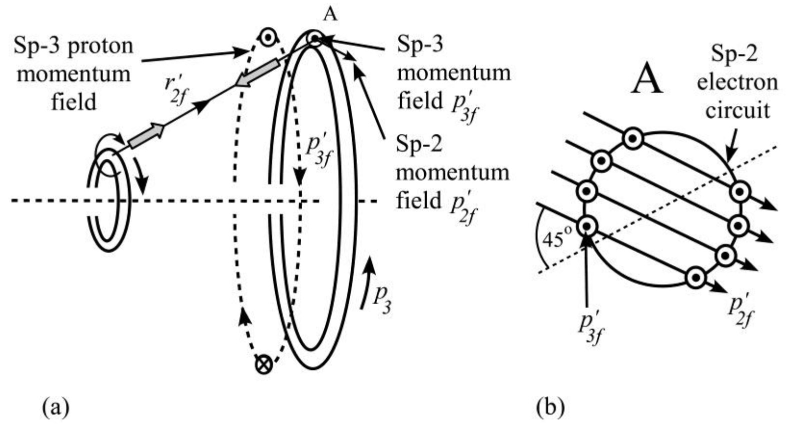

Figure 4. A schematic representation of the proton momentum field components (not to scale). **a** The proton field source (left) generates an electric momentum field p'_{3f} (dots/crosses) that can penetrate a target PTV (right). The field p'_{3f} and resident momenta p_3 in the target rotate in opposition as an attraction interaction. **b** The proton also generates a magnetic momentum field p'_{2f}. In the parallel field approximation, these vectors are treated as approximately parallel in the locality of the target Sp-2 circuit.

The PTV model proposes that both Sp-2 (poloidal) and Sp-3 (toroidal) rotations generate momentum fields in the surrounding space, though the complete dynamics of the field are not fully specified in Ref. [4]. As the PTV rotates, momentum field emissions occur continuously from the curvature of the Sp-1 helical trajectory in both Sp-2 and Sp-3 motion. The electron's Sp-2 magnetic momentum field p_{2f} and its Sp-3 electric momentum field p_{3f} are mutually perpendicular components of the total momentum field. Following the approach in Ref. [4, Eqs. (25), (26), (45) and (46)] in which we allow the field *speed* to diminish with r_{2f} while the field mass remains invariant, and for the electron we adopt the field momentum magnitudes:[5]

$$p_{2f} = \frac{\hbar}{r_{2f}} = m_o c \frac{r_{2o}}{r_{2f}}, \qquad p_{3f} = m_o \frac{\alpha c}{Y} \frac{r_{2o}}{r_{2f}} \tag{9}$$

where $r_{2f} = r'_{2f}$ is the field radius from the Sp-2 center, α is the fine structure constant, and $Y = n_r + \left(n_\phi^2 - \alpha^2\right)^{1/2}$.[6] For the proton, $Y = (1 - \alpha^2)^{1/2}$. From Eq. (9), the field components maintain their relationship as they propagate through space:

$$p_{3f} = p_{2f} \frac{\alpha}{Y} \tag{10}$$

The continuous generation of field emissions is formally unbound within the model though only a portion of field that interacts with the Sp-2 rotational geometry becomes accessible. The field otherwise remains undetected.

We now consider the parallel field approximation. The spiral field geometry in Ref. [4, Fig. 11] suggests that the proton magnetic momentum field vectors $\vec{p}'_{2f}$ actually arrive at 45° to the line joining the proton-electron Sp-2 centers due to the field emission mechanism.[7] Here, the field momentum $\vec{p}'_{2f}$ is to be given two degrees of freedom in the plane perpendicular to the proton's poloidal axis: radial and azimuthal (Sp-2 rotational) mo-

---

[5] Note when $r_{2f} = r'_{2f} = r_{2o}$, we must have $p_{2f} = m_o c$ and $p_{3f} = m_o \alpha c / Y$. Also, from Ref. [4, Eq. (23)] we have $\hbar = m_o c r_{2o} = m_o \alpha c r_{3o} / (1 - \alpha^2)^{1/2}$ for the unloaded case using Eq. (7).

[6] The azimuthal n_ϕ and radial n_r quantum numbers follow Sommerfeld's scheme [11–12].

[7] The mechanism involves equal partitioning between radial and azimuthal momentum at the point of emission to create the 45° spiral angle that is preserved during propagation. In fact, Ref. [4, Fig. 11a] should show the $\vec{p}'_{2f}$ vectors as being at 45° to the Sp-2 tangent.

mentum. We assume equal partitioning between these components such that each carries magnitude $\hbar/(\sqrt{2}r'_{2f})$. Only the Sp-2 azimuthal component of the field participates in the magnetic coupling. A pure radial field and a pure azimuthal field would both produce a zero line integral around a circuit. In the parallel field approximation, the field orientation remains constant at the two points where any radial line from the proton center intersects the electron circuit. This eliminates the geometric compensation present in pure azimuthal fields, where two different alignment angles on this radial line exactly cancel the 1/r magnitude variation. With constant field orientation — see p'_{2f} in Eq. (27) — only the magnitude varies, producing a net non-zero line integral proportional to the integrated field strength around the electron Sp-2 circuit. As we shall in Sec. 3.4, the $1:1$ ratio between radial and azimuthal momentum may represent a fundamental constraint on field geometries capable of generating magnetic coupling. This non-cancelling geometry is essential: without the radial momentum component that straightens the spiral and enables the parallel field approximation, the line integral would vanish as it does for purely radial and purely azimuthal fields.

2. Methodology

2.1. PTV calculations

The calculation obtains the Sp-3 rotation frequencies of the electron toroid. Transition frequencies are the differences between them. An emission results from the transition from a low frequency level (high n) to a high frequency state (low n) emitting a circularly polarized or optical OAM ray that rotates in opposition to the Sp-3 rotation. The unadjusted fine structure is calculated from Ref. [4, Eq. (51)] with a conversion from energy (J) to frequency (MHz).

The center of mass is located on the rotating line joining the centers of the proton and electron Sp-2 circuits and is transformed to the proton rest-mass frame so that the speed of the electron relative to the proton is obtained, see Sec. 3.2. The consequent frequency obtained is ν_{3D}, see Eqs. (12) and (13). This is the adjusted fine structure frequency indicated in Figs. 5 and 6. The mechanism for this depends on the relative proton–electron Sp-2 rotation senses. There are two cases that are set out in Table I: (a) the proton–electron Sp-2 have the same sense so that a reduction is imposed on the proton Sp-2 frequency ($\Gamma > 0$); or (b) they are opposite sense in which case an increase is imposed ($\Gamma < 0$). For (a), the result is an extraction of action from the proton Sp-3 rotation to restore the Sp-2 action, so that the proton advances towards the electron, see Eq. (13). With (b), the extra Sp-2 action is displaced into the proton Sp-3 and so it retreats from the electron, see Eq. (13).[8] However, there is also a red shift or blue shift $\Delta\nu_{shift}$ that needs to be accounted for that targets the hyperfine midpoint frequency, in which the A and B are empirically determined constants, see Eq. (22) with Tables II and III. This is the 'magnetic potential adjustment' calculation in Sec. 3.3. While the traditional Lamb shift calculation aims for the centroid for the hyperfine states, the PTV method targets the mid-point of the two values in the absence of an external field. So, the magnetic potential in Eq. (22) is analogous to the Lamb shift calculation and is shown in Figs. 5 and 6.

Comparison of the traditional Lamb shift frequency in Fig. 1 with the PTV magnetic potential shifts in Figs. 5 and 6 shows that the PTV shift to be accounted for is far greater. The hyperfine shift also depends on the relative rotation senses of the proton-electron Sp-2 circuits, in which the electron Sp-2 energy is raised or lowered by the same frequency $\Delta\nu_{hf}$ about the hyperfine mid-point, see Eq. (35). However, there is an assumption that is vital to the hyperfine calculation. While the proton Sp-2 field is generated continuously as

---

[8] The attraction and repulsion mechanisms are explained in Ref. [4, Sec. 4.1].

the proton structure rotates, we assume that in the locality of the electron Sp-2 circuit, the field momentum vectors are approximately parallel, at 45° to the line joining the Sp-2 centers, and lying in the plane of the electron Sp-2 circuit, see Fig. 4b. The parallel-field approximation is validated by the $k = 1$ requirement from Table VII for the $nS_{1/2}$ states in Eq. (35) as this represents no adjustment.

The raising or lowering of the hyperfine mid-point occurs because the motion of the electron towards the proton results in a *change* in the proton's Sp-2 momentum field integrated around the electron Sp-2 circuit. This energy is redistributed into Sp-3 motion. In summary, the full calculation for the pair of hyperfine frequencies is as follows, see also Eq. (50):

$$\Delta\nu_{final} = \nu_{3D} + \Delta\nu_{shift} + \Delta\nu_{hf} \tag{11}$$

Here, $\Delta\nu_{hf}$ and $\Delta\nu_{shift}$ and are both negative for $\Gamma > 0$ (see Fig. 5), and both positive when $\Gamma < 0$ (see Fig. 6). The shifts applied to the adjusted fine structure ν_{3D} are given by Eqs. (12) and (13) and are summarized in Table 1.

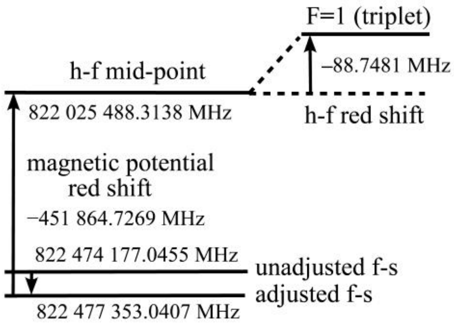

Figure 5. The $2S_{1/2}$ state of hydrogen calculated from the PTV model with $\Gamma > 0$, see Appendix B. The unadjusted fine structure frequency (MHz) with no reduced mass is shown from Ref. [4, Eq. (51)]. The adjusted fine structure frequency ν_{3D}, including the state-dependent reduced mass and proton-speed correction, is shown from Eqs. (12) and (13). The 'magnetic potential' red shift $\Delta\nu_{shift}$ is calculated from Eq. (22) and Table II to reach the hyperfine mid-point. The hyperfine shift $\Delta\nu_{hf}$ from the mid-point is calculated from Eq. (35).

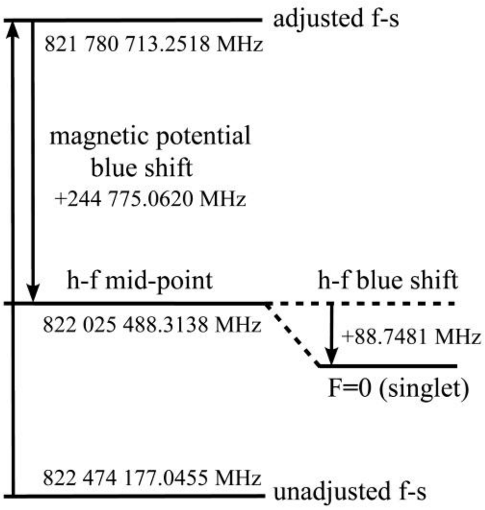

Figure 6. The $2S_{1/2}$ state of hydrogen calculated from the PTV model with $\Gamma < 0$. The unadjusted fine structure frequency (MHz) with no reduced mass is shown from Ref. [4, Eq. (51)]. The adjusted fine structure frequency ν_{3D}, including the state-dependent reduced mass and proton-speed correction, is shown from Eqs. (12) and (13). The 'magnetic potential' blue shift $\Delta\nu_{shift}$ is calculated

from Eq. (22) and Table III to reach the hyperfine mid-point. The hyperfine shift $\Delta\nu_{hf}$ from the mid-point is calculated from Eq. (35).

From Tables II and III, the value and sign of A in Eq. (22) turns out to be related to that of Γ — see Sec. 3.2 and Eq. (37). So with $B \sim -3.000$ across all states, Eq. (22) has the character of a magnetic dipole-dipole interaction. So we shall refer to Eq. (22) as a 'magnetic potential adjustment' that results from the interaction of the proton Sp-2 field on the electron, one that is in need of further investigation. In fact, the connection between A and Γ extends also to deuterium (Tables XI and XII), tritium (Table XV), and $^{3}He^{+}$ (Table XVI) which leads to our proposal of a universal nuclear scaling law in Eq. (37).

The full calculation for the $2S_{1/2}$ state with $\Gamma > 0$ appears in Appendix B with the results represented in Fig. 5.

Table I. How the relative proton–electron Sp-2 rotation senses determine the sign of Γ in Eq. (13), the effect on the proton motion in the center of mass frame, the electron fine structure energy ν_{3D} in Eq. (12), the hyperfine shift in Eq. (35), and the magnetic potential shift in Eq. (22).

relative Sp-2 senses	**Γ sign**	**proton motion**	$\boldsymbol{\nu_{3D}}$	**hyperfine shift**	**mag. pot. shift**
same	+	towards electron	increases	red	red
opposite	−	away from electron	decreases	blue	blue

2.2. Comparison with QED

The PTV approach trades mathematical accuracy for conceptual clarity. While the D-function — Eq. (13) — and the k multipliers — Table VII and Eq. (35) — are empirically determined, they are consequences of a geometrical model. The magnetic potential — Tables II and III with Eq. (22) — needs further investigation but it results from the effect of the proton Sp-2 momentum field on the electron Sp-2 circuit. PTV theory provides a calculation that uses the same equations for each (n_r, n_ϕ) combination. These calculations can be performed on an electronic calculator across 30 pairs of hyperfine frequencies for each of the two signs of Γ featuring the first six states for each of $nS_{1/2}$, $nP_{1/2}$, $nP_{3/2}$, $nD_{3/2}$, and $nD_{3/2}$, see Appendix B.

PTV calculation [4, Eq. (51)]

(1) Modified fine structure equation, Eqs. (12) and (13)
(2) Bound state proton-electron displacement [4, Eq. (85) and Table 2]
(3) State-dependent reduced mass correction, Eq. (13)
(4) Relative-to-proton speed adjustment, Eqs. (12) and (13)
(5) Radiation exit potential, Eq. (22) with Tables II and III
(6) Hyperfine shift, Eq. (35)

QED calculation [17; 18, Sec. 3.1.1]

(1) Dirac equation solution
(2) Self-energy correction (multi-loop integrals)
(3) Uehling potential shift
(4) Wichmann-Kroll corrections
(5) Higher-order radiative corrections in α/π
(6) Nuclear size corrections to the Dirac energy
(7) Relativistic recoil correction
(8) Relativistic reduced mass correction

Considering mean absolute errors, QED's hyperfine splitting accuracy is ~ 30 times more accurate than PTV, however, the PTV median is only 0.0015 MHz against the QED median of 0.0000 MHz based on 16 states, see Table X. The PTV's Lamb shift accuracy is ~ 40 times more accurate than QED, see Table IX. However, they are not accounting for the same frequency difference, the PTV difference being ~ 30 times the QED difference for the $2S_{1/2}$ state. Since PTV uses the same basic equations for each state, its computational task represents a 10-fold reduction in complexity. The comparative errors are given in Sec. 4.

3. Hydrogen PTV

3.1. Fine structure corrections

Analogous to the Lamb shift calculations in QED, there are also correction terms for the PTV model: the proton speed adjustment, and the magnetic potential adjustment. These are both empirical formulae and unlike QED which aims for the hyperfine centroid, in PTV theory we target the mid-point of the hyperfine pair. Equation (12) shows the fine structure formula from PTV theory [4, Eq. (51)] modified by the relative-to-proton speed adjustment D, and the state-dependent reduced mass M_r in Eq. (13). Equation (22) is then used for the magnetic potential adjustment. An approximately equal blue or red shift about the hyperfine mid-point — depending on the proton–electron Sp-2 rotation senses — produces the hyperfine splitting, see Eq. (35). In the following calculations, frequencies ν (MHz) are obtained from the given energies ε with a multiplication by $10^{-6}/h$.

3.2. Relative-to-proton speed adjustment

We now posit a modification function $D = D(n)$ to the fine structure energy in Ref. [4, Eq. (51)] which takes the speed that the electron is advancing towards the proton and either adds ($\Gamma > 0$) or subtracts ($\Gamma < 0$) the proton speed.[9]

$$\nu_{3D} = \frac{m_o 10^{-6}}{(1+M_r)h\left(1-\dfrac{\alpha^2 D}{2Y_D^2\left(1+\dfrac{\alpha^2 D}{Y_D^2}\right)}\right)^{1/2}} \frac{\alpha^2 c^2}{2Y_D^2\left(1+\dfrac{\alpha^2}{Y_D^2}\right)} D \tag{12}$$

with the adjustment $Y_D = n_r + \left(n_\phi^2 - \alpha^2 D\right)^{1/2}$, $n = (n_\phi + n_r)$. Here, we posit that

$$D = \left(1+\frac{\Gamma M}{n}\right)^2, \quad M_r = \frac{m_o}{m_o'\left(1-\dfrac{\alpha^2}{2Y^2\left(1+\dfrac{\alpha^2}{Y^2}\right)}\right)^{1/2}} \tag{13}$$

where Γ is an empirically determined multiplier.[10] In Eq. (13), the M in the D-function, or more specifically the electron rest mass, does not merit relativistic adjustment to M_r because the D-function is a pure Sp-2 effect whereas a relativistic component has its origin in Sp-3 rotation. The D-function is introduced to represent the cumulative back-reaction of the electron Sp-2 momentum circulation on the proton Sp-2 momentum field. Here, momentum fields are reciprocal, and any interaction that produces an accumulated effect on the electron Sp-2 circuit must produce a corresponding modification of the proton's internal circuit. The tentative derivation that follows intended to establish the expected scaling and bounded nature of this response rather than to provide a first-principles electrodynamics derivation.

We need to find the proton speed along r_{2f} in the center of mass frame. Our interest is in the p_{2f} momentum field generated by the electron that impinges on the proton Sp-2 circuit since this will affect the Sp-3 momentum which in turn affects the linear momentum along r_{2f}. First, we make the assumption that in any electron Sp-2 time period T_2

---

[9] Any occurrence of α^2 is replaced by $\alpha^2 D$.

[10] See Sec. 3.3 for the conditions for optimizing Γ.

only one of the electron momentum field emissions from the $n_\phi^2 n^2$ electron Sp-2 circuits [4, Fig. 13] — where $n_\phi = 1$ for the $nS_{1/2}$ states — manages to strike the proton.[11] This means that the Sp-2 field momentum the proton receives depends on $\hbar/n^2$. So, from Eqs. (9) and Ref. [4, Eq. (72)], we have

$$p_{3f} = \frac{\hbar\alpha}{n^2 r_{2f} Y} \tag{14}$$

The total-action integral for the proton Sp-2 circuit is as follows [4, Eq. (73)]:

$$J_{3f} = \int_{\gamma=0}^{\gamma=2\pi} \vec{p}_{3f} \cdot d\vec{r}_2' = \int_0^{2\pi} \frac{\hbar\alpha}{n^2 r_{2f} Y} \begin{pmatrix} -\sin\gamma \\ \cos\gamma \\ 0 \end{pmatrix} \cdot r_{2o}' d\gamma \begin{pmatrix} -\sin\gamma \\ \cos\gamma \\ 0 \end{pmatrix} \tag{15}$$

To obtain the field energy inhabiting the proton PTV we divide by the electron time period for a single Sp-2 circuit ($n = 1$) because the electron PTV energy displaced into energy of motion is also based on that. This is [4, Eq. (79)][12]

$$T_2 = \frac{2\pi r_{2o}\left(1 + \frac{\alpha^2}{Y^2}\right)^{1/2}}{c} \tag{16}$$

So finally, the proton PTV energy taken into or displaced out of its Sp-2 rotation is

$$\varepsilon_{3f} \sim \frac{\hbar\alpha c r_{2o}'}{2\pi n^2 Y r_{2o}} \int_0^{2\pi} \frac{d\gamma}{r_{2f}} \sim \frac{m_o \alpha^2 c^2 r_{2o}'}{n^2 \bar{d}_2 Y r_{2o}} \tag{17}$$

Here, we have made use of $\hbar = m_o \alpha c r_{3o}$ [4, Eq. (23)] with $m_2 \sim m_o$, and the proton-electron normalized bound-state distance $r_{2f}/r_{3o} \sim \bar{d}_2$ [4, Eqs. (77), (84), and (86)]. Since $r_{2o}'/r_{2o} = M$ [4, Eq. (84)], $Y \sim n$, and $\bar{d}_2 \sim 2n$ [4, Table 2] we arrive at

$$\varepsilon_{3f} \sim \frac{m_o' \alpha^2 c^2 M^2}{2n^4} \tag{18}$$

where m_o' is the proton rest mass and $M = m_o/m_o'$. We now refer back to the form of the Sp-3 energy in Eq. (8). To produce the proton speed along r_{2f} towards the electron in the center of mass frame, we divide by m_o' and effect a square root so that

$$v' \sim \frac{\alpha c M}{\sqrt{2} n^2} \tag{19}$$

Now, the speed of the electron towards the proton along r_{2f} in the center of mass frame is [4, Eq. (50)]

$$v \sim \frac{\alpha c}{\sqrt{2} Y} \tag{20}$$

which means that the speed adjustment in relation to the proton rest frame with $Y \sim n$ is

$$\frac{v}{c} \to \frac{\alpha}{\sqrt{2} Y}\left(1 + \frac{M}{n}\right) \tag{21}$$

So in the fine structure formula [4, Eq. (51)], $\alpha^2/2Y^2$ is everywhere replaced by the square of Eq. (21) to produce Eq. (12). We should expect there to be two cases: $\Gamma > 0$ producing a fine-structure frequency reduction and an increase in relative proton-electron

---

[11] This is a reasonable assumption concerning phase relationship. In Ref. [4, Fig. 13a], as the interlaced helical strings progress together from left to right, points at the same height in the diagram are reached at time intervals of T_2/n. If one point generates a momentum field that strikes the proton, the proton will have moved on by the time the next point on the electron Sp-2 structure is ready to generate a field.

[12] In Ref. [4, Eq. (79)] the given time period is the time required to traverse the whole structure and should have n instead of n^2 since there are n wavelengths to traverse by the n interlacings.

speed; and $\Gamma < 0$ giving an increase in frequency and a movement of the proton away from the electron. The case depends on the combination of proton-electron Sp-2 rotation senses.[13] The *theoretical* exploration of Γ is beyond the scope of the present work, suffice it to say that for $\Gamma \sim 1$ reasonable agreement with the reduced-frequency Lamb shift is obtained for $nS_{1/2}$ states, see Table II.

3.3. Magnetic potential adjustment

Whereas QED calculations aim to bridge the discrepancy between the reduced-mass fine structure level and the hyperfine centroid [17], the calculation in the proposed PTV model aims for the mid-point frequency of the two hyperfine states. The changing proton momentum field interaction with the two Sp-2 rotation senses of the electron poloidal circuit then raises or lowers the mid-point frequency by an equal magnitude to give the two hyperfine frequencies, see Sec. 3.4 with Fig. 5 and 6. However, we suggest that there is also an effect of the proton magnetic momentum field (Sp-2) in the locality of the electron Sp-2 that we shall denote as the 'magnetic potential adjustment'. This should also have a red shift or blue shift effect depending on the proton-electron Sp-2 rotation senses, see Table I. Although the form of Eq. (22) resembles that of a static magnetic dipole-dipole potential, within the PTV framework it is more appropriately interpreted as a cumulative interaction energy. As the electron Sp-2 circuit approaches the proton from infinity, it traverses a spatially varying magnetic momentum field generated by the proton's Sp-2 rotation. The work done by this field accumulates along the approach trajectory, resulting in a net frequency displacement at the bound state separation. This accumulated effect depends on the bound-state separation but does not involve time-periodic energy transfer once the bound state is established.

To span the gap between the adjusted fine-structure prediction in Eq. (12) and the hyperfine mid-point, the 'magnetic potential adjustment' is cast in the form of Eq. (22), where $\bar{d}_2$ is the normalised bound-state distance between the centers of the electron and proton Sp-2 poloidal rotations [4, Eq. (86) and Table 2].[14] Ref. [4, Eq. (80)] obtains the Coulomb energy on the assumption that it is inversely proportional to the total quantum number n. This leads to a model in which the shortest distance between the proton and electron Sp-2 centers $\bar{d}_2 \sim 2n$, see Ref. [4, Table 2]. So, the adjustment is as follows:

$$\Delta\nu_{shift} = A\bar{d}_2^B \tag{22}$$

where A and B are constants to be determined empirically.

Figures 5 and 6 exhibit $\Delta\nu_{shift}$ as the difference between the adjusted fine structure frequency, given by Eqs. (12) and (13), and the hyperfine mid-point.

Table II. The optimized radiation exit red shift constants (A, B) in Eq. (22) for 30 states of hydrogen $nS_{1/2}$, $nP_{1/2}$, $nP_{3/2}$, $nD_{3/2}$, and $nD_{5/2}$, for $\Gamma > 0$ in Eq. (13).

States	***A* (MHz)**	***B***	**Γ**	**A/Γ (MHz)**
$nS_{1/2}$	−28 923 705.165 63	−3.000 042 185 959 5	1.006 942 7	−28 724 281.1
$nP_{1/2}$	−15 981 616.616 9	−3.000 009 463 84	0.557 738 902 61	−28 654 297.8
$nP_{3/2}$	−14 008 000.638 5	−3.000 009 763 61	0.488 785 369 95	−28 658 796.9
$nD_{3/2}$	−11 341 280.037 6	−3.000 004 673 972	0.395 775 5	−28 655 841.6
$nD_{5/2}$	−10 734 985.134 8	−3.000 004 778 242	0.374 597 05	−28 657 420.4

---

[13] The reasoning here is that if the proton Sp-2 frequency is reduced with $\Gamma > 0$, the momentum is removed from the Sp-3 rotation to compensate for the loss of action. The proton must move towards the electron to reduce the Sp-3 action to its next stable value, see also Ref. [4, Sec. 2.6].

[14] Normalisation here means a division by r_{3_0} the invariant electron Sp-3 radius (same for all states).

The D-function in Eqs. (12) and (13) has been empirically determined with the aim of obtaining the greatest consistency in the A and B constants in Tables II and III for Eq. (22). For a particular set of six states, for example $nS_{1/2}$, we take the experimental $\Delta\nu_{diff}$ — the absolute difference between Eq. (12) and the experimental hyperfine mid-point [20, Tables III, IV, V] — and the bound state separation $\bar{d}_2$ for successive states [4, Table 2]. The values of $\Delta\nu_{diff}$ are to be equalled by $\Delta\nu_{shift}$ in Eq. (22). Taking the logarithm of Eq. (22), we set up a B gradient

$$B_{n,n+1} = \frac{\log\left(\Delta\nu_{diff}\right)_{n+1} - \log\,(\Delta\nu_{diff})_n}{\log\,(\bar{d}_2)_{n+1} - \log\,(\bar{d}_2)_n}, \tag{23}$$

Table III. The optimized radiation exit blue shift constants (A, B) in Eq. (22) for 30 states of hydrogen $nS_{1/2}$, $nP_{1/2}$, $nP_{3/2}$, $nD_{3/2}$, and $nD_{5/2}$, for $\Gamma < 0$ in Eqs. (13).

States	**A (MHz)**	**B**	**Γ**	**A/Γ (MHz)**
$nS_{1/2}$	15 666 540.393 06	−2.999 976 494 243	−0.549 012	−28 535 879.7
$nP_{1/2}$	5 870 876.745 0	−3.000 001 596 923	−0.204 816 440 02	−28 664 089.4
$nP_{3/2}$	6 693 635.451	−3.000 002 303 498	−0.233 610 142 41	−28 653 017.3
$nD_{3/2}$	5 263 782.149	−3.000 002 402 484	−0.183 673 5	−28 658 364.7
$nD_{5/2}$	5 590 077.322 6	−3.000 002 371 7	−0.195 081 1	−28 655 145.6

The difference in gradients $(B_{n+1,n+2} - B_{n,n+1})$ — formed from the lowest three states of the set — is then minimized by searching through values of Γ in the D function. The $B_{n,n+1}$ for the lowest pair of the set is used to represent the whole set — for example, $n = 1$ for $nS_{1/2}$. Once B is established, we return to Eq. (22) and search for the A that minimizes the deviation of Eq. (12) from the lowest n experimental hyperfine midpoint.[15] This produces errors < 0.1 kHz for the first three states of each set, see Tables IV and V. It turns out that $B \sim -3$ across all 30 states tested, see Tables II and III. This suggests something more significant than curve fitting and that a fundamental mechanical process is at work. In fact, the r^{-3} power law hints at a magnetic dipole-dipole interaction.

Table IV. Hydrogen hyperfine mid-point results for the case $\Gamma > 0$, with the $nS_{1/2}$ states $(n = 1, 2, \ldots, 6)$, $nP_{1/2}$ states $(n = 2, 3, \ldots, 7)$, $nP_{3/2}$ states $(n = 2, 3, \ldots, 7)$, $nD_{3/2}$ states $(n = 3, 4, \ldots, 8)$, and $nD_{5/2}$ states $(n = 3, 4, \ldots, 8)$. The experimental values ν_{exp} [20, Tables III, IV, V] are the top values, and the optimized values given by Eqs. (12), (13), (22) and Table II are the lower values.

State	**ν_{exp} (MHz) $(\nu_{3D} - \Delta\nu_{shift})$**	**$\Delta\nu_{err}$ (MHz)**	**State**	**ν_{exp} (MHz) $(\nu_{3D} - \Delta\nu_{shift})$**	**$\Delta\nu_{err}$ (MHz)**
$1S_{1/2}$	3 288 087 212.213 1 3 288 087 212.213 1	0.000 0	$5P_{3/2}$	131 522 538.831 8 131 522 538.834 3	0.002 6
$2S_{1/2}$	822 025 488.313 8 822 025 488.313 8	0.000 0	$6P_{3/2}$	91 335 060.003 3 91 335 060.007 2	0.003 9
$3S_{1/2}$	365 343 591.599 6 365 343 591.599 6	0.000 0	$7P_{3/2}$	67 103 286.639 9 67 103 286.644 2	0.004 3
$4S_{1/2}$	205 505 298.855 2 205 505 298.951 0	0.095 8	$3D_{3/2}$	365 340 649.089 8 365 340 649.089 8	0.000 0
$5S_{1/2}$	131 523 175.306 4 131 523 175.425 8	0.119 4	$4D_{3/2}$	205 504 057.762 2 205 504 057.762 2	0.000 0
$6S_{1/2}$	91 335 428.313 7 91 335 428.428 0	0.114 4	$5D_{3/2}$	131 522 539.938 1 131 522 539.938 1	0.000 0
$2P_{1/2}$	822 026 516.551 2 822 026 516.551 2	0.000 0	$6D_{3/2}$	91 335 060.647 2 91 335 060.647 5	0.000 3
$3P_{1/2}$	365 343 897.705 1 365 343 897.705 1	0.000 0	$7D_{3/2}$	67 103 287.046 9 67 103 287.047 2	0.000 6
$4P_{1/2}$	205 505 428.231 8 205 505 428.231 8	0.000 0	$8D_{3/2}$	51 375 939.517 4 51 375 939.518 2	0.000 8
$5P_{1/2}$	131 523 241.6071	0.002 9	$3D_{5/2}$	365 339 565.452 0	0.000 0

---

[15] The errors are greatest for the lowest state of the set so this is the focus when optimizing A.

	131 523 241.610 0			365 339 565.452 0	
$6P_{1/2}$	91 335 466.701 5 91 335 466.705 9	0.004 4	$4D_{5/2}$	205 503 600.601 9 205 503 600.601 9	0.000 0
$7P_{1/2}$	67 103 542.752 6 67 103 542.757 7	0.005 1	$5D_{5/2}$	131 522 305.872 0 131 522 305.872 0	0.000 0
$2P_{3/2}$	822 015 535.670 9 822 015 535.670 9	0.0000	$6D_{5/2}$	91 334 925.192 3 91 334 925.192 6	0.000 4
$3P_{3/2}$	365 340 644.108 0 365 340 644.108 0	0.000 0	$7D_{5/2}$	67 103 201.745 8 67 103 201.746 4	0.000 6
$4P_{3/2}$	205 504 055.622 2 205 504 055.622 2	0.000 0	$8D_{5/2}$	51 375 882.372 4 51 375 882.373 2	0.000 8

The consistency of the results for both B and A/Γ in Tables II and III is notable. It turns out that the mean value of the latter is $\mathrm{A}/\Gamma = -28{,}651{,}713$ MHz over the 10 sets of states. In examining the cases for deuterium, tritium, $^{3}\mathrm{He}^{+}$, and $^{7}\mathrm{Li}^{2+}$, this value plays a crucial role in a new empirical law, see Eq. (37).

Each of the following series has its own pair of constants A and B: $nS_{1/2}$ $(n = 1,2,\ldots,6)$, $nP_{1/2}$ $(n = 2,3,\ldots,7)$, $nP_{3/2}$ $(n = 2,3,\ldots,7)$, $nD_{3/2}$ $(n = 3,4,\ldots,8)$, and $nD_{5/2}$ $(n = 3,4,\ldots,8)$. So, after the optimum values (A,B) for ν_{3D} and $\Delta\nu_{shift}$ have been ascertained, we compute the error magnitude $\Delta\nu_{err}$ from experiment [20] as follows:

$$\Delta\nu_{err} = |\nu_{exp} - \nu_{3D} - \Delta\nu_{shift}| \tag{24}$$

Tables IV and V show the optimized errors $\Delta\nu_{err}$ of PTV theory from experiment for various states. The values of (A,B) in Eq. (22) are given in Tables II and III.

Table V. Hydrogen hyperfine mid-point results for the blue shift $\Gamma < 0$, with the $nS_{1/2}$ states $(n = 1,2,\ldots,6)$, $nP_{1/2}$ states $(n = 2,3,\ldots,7)$, $nP_{3/2}$ states $(n = 2,3,\ldots,7)$, $nD_{3/2}$ states $(n = 3,4,\ldots,8)$, and $nD_{5/2}$ states $(n = 3,4,\ldots,8)$. The experimental values ν_{exp} [20, Tables III, IV, V] are the top values, and the optimized values given by Eqs. (12), (13), (22) with Table II are the lower values.

State	$\boldsymbol{\nu_{exp}}$ **(MHz)** $(\boldsymbol{\nu_{3D} - \Delta\nu_{shift}})$	$\boldsymbol{\Delta\nu_{err}}$ **(MHz)**	**State**	$\boldsymbol{\nu_{exp}}$ **(MHz)** $(\boldsymbol{\nu_{3D} - \Delta\nu_{shift}})$	$\boldsymbol{\Delta\nu_{err}}$ **(MHz)**
$1S_{1/2}$	3 288 087 212.213 1 3 288 087 212.213 1	0.000 0	$5P_{3/2}$	131 522 538.831 8 131 522 538.830 8	0.001 0
$2S_{1/2}$	822 025 488.313 8 822 025 488.313 8	0.000 0	$6P_{3/2}$	91 335 060.003 3 91 335 060.001 8	0.001 5
$3S_{1/2}$	365 343 591.599 6 365 343 591.599 6	0.000 0	$7P_{3/2}$	67 103 286.639 9 67 103 286.638 3	0.001 6
$4S_{1/2}$	205 505 298.855 2 205 505 298.864 1	0.008 9	$3D_{3/2}$	365 340 649.089 8 365 340 649.089 8	0.000 0
$5S_{1/2}$	131 523 175.306 4 131 523 175.320 5	0.014 1	$4D_{3/2}$	205 504 057.762 2 205 504 057.762 2	0.000 0
$6S_{1/2}$	91 335 428.313 7 91 335 428.329 2	0.015 5	$5D_{3/2}$	131 522 539.938 1 131 522 539.938 1	0.000 0
$2P_{1/2}$	822 026 516.551 2 822 026 516.551 2	0.000 0	$6D_{3/2}$	91 335 060.647 2 91 335 060.647 0	0.000 2
$3P_{1/2}$	365 343 897.705 1 365 343 897.705 1	0.000 0	$7D_{3/2}$	67 103 287.046 9 67 103 287.046 6	0.000 2
$4P_{1/2}$	205 505 428.231 8 205 505 428.231 8	0.000 0	$8D_{3/2}$	51 375 939.517 4 51 375 939.517 2	0.000 2
$5P_{1/2}$	131 523 241.607 1 131 523 241.606 2	0.000 9	$3D_{5/2}$	365 339 565.452 0 365 339 565.452 0	0.000 0
$6P_{1/2}$	91 335 466.701 5 91 335 466.700 2	0.001 3	$4D_{5/2}$	205 503 600.601 9 205 503 600.601 9	0.000 0
$7P_{1/2}$	67 103 542.752 6 67 103 542.751 4	0.001 1	$5D_{5/2}$	131 522 305.872 0 131 522 305.872 0	0.000 0
$2P_{3/2}$	822 015 535.670 9 822 015 535.670 9	0.0000	$6D_{5/2}$	91 334 925.192 3 91 334 925.192 1	0.000 1
$3P_{3/2}$	365 340 644.108 0 365 340 644.108 0	0.000 0	$7D_{5/2}$	67 103 201.745 8 67 103 201.745 6	0.000 2
$4P_{3/2}$	205 504 055.622 2 205 504 055.622 2	0.000 0	$8D_{5/2}$	51 375 882.372 4 51 375 882.372 1	0.000 3

3.4. Hyperfine splitting mechanism

It is important to distinguish the cumulative magnetic interaction embodied in Eq. (22) from the hyperfine splitting mechanism describe here. Whereas the magnetic potential adjustment reflects an internal accumulation with respect to separation distance during the formation of the bound state, the hyperfine splitting arises from a local, time-periodic interaction at fixed bound-state separation. The latter produces distinct steady-state eigenvalues associated with different relative Sp-2 rotation senses, rather than an accumulated energy transfer over successive time periods. The magnetic potential appears static because the spatial integration of the proton Sp-2 momentum-field gradient cancels the spatial differentiation that generates it, leaving an endpoint-dependent energy offset. In contrast, the hyperfine splitting arises because the time integration over a Sp-2 period does not cancel the underlying spatial field gradient, resulting in distinct steady state eigenvalues.

There are n^2 electron Sp-2 circuits in each of n_ϕ^2 strings [4, Eq. (72) and Fig. 13]. In each of the n_ϕ^2 strings, the energy gained or lost by all the sub-string field momentum absorptions is the sum over the n^2 circuits. So, each of the n_ϕ^2 strings —consisting of n interlaced components, each with n wavelengths — receives the same field momentum change but the energies gained or lost are not summed over the n_ϕ^2 strings. Instead, they are to be treated as components of an intensity, each being available to affect a detector individually. Coincidences occur with low probability, so they are regarded as separate but equal energies (for a discussion of this point see Ref. [21]).

Figure 4 shows the proton momentum fields. Consider a half plane containing the common toroidal axis — dotted in Fig. 4a — and the length r_{2f}' joining the center of the proton Sp-2 circuit with a point on the electron Sp-2 circuit A. The proton's electric or Sp-3 field momentum p_{3f}' is perpendicular to the half-plane while its magnetic or Sp-2 field momentum p_{2f}' lies in the half-plane. We shall assume that in the vicinity of the electron all Sp-2 momentum vectors $\vec{p}_{2f}'$ are approximately parallel, in the plane of the electron Sp-2 circuit, and 45° to the line joining the Sp-2 centers of A and B, see Fig. 4b. This bound-state distance joining the Sp-2 centers we have denoted as $\bar{d}_2$, which has been normalised with a division by r_{3o} [4, Eq. (86)].

Now that we have calculated the mid-point of the two hyperfine levels for all states — see Tables IV and V — it remains to vary the Sp-2 rotation senses with the electron approaching the proton, to either reduce or increase this hyperfine mid-point frequency by the same magnitude and thereby obtain the two hyperfine frequencies, see Table I.[16] In the formation of a bound state, whether the proton is induced to move towards or away from the electron, the latter's speed is always much greater than the former so that they are always converging. The separation of hyperfine levels in an external field will not be considered here.

We now propose a PTV model for electromagnetic induction. For the treatment of the proton magnetic-momentum field that follows, there needs to be a change in the proton's Sp-2 field momentum p_{2f}' cutting the Sp-2 electron circuit in order to generate a change in energy, see Fig. 4b. This is occasioned by a movement of the electron Sp-2 circuit A through the proton field along r_{2f}', see Fig. 4a. The proton's Sp-2 field gradient means that the near side of the electron's Sp-2 circuit experiences a stronger field to the far side resulting in a net torque.[17] Since the electron Sp-2 action must remain constant then the excess or deficit of momentum is redistributed into or drawn from the Sp-3 action, and

---

[16] Of course, both the proton and electron Sp-2 rotation senses each have two possibilities.

[17] Oppositely-directed momenta involving field and circuit at this strong point means a net reduction in the target Sp-2 circuit, while same-directed momenta leads to a gain around the circuit.

subsequently contributes to the electron momentum along r'_{2f} towards the proton in a helical trajectory on the surface of a frustrum.[18] This forms the energy available for emission at the state boundary.[19] In respect of the proton–electron Sp-2 rotations, Table VI shows the four combinations of same and opposite sense rotations with the proton and electron either approaching or receding, together with the resulting increase (higher hyperfine) or decrease (lower hyperfine) in frequency. We are only interested in the convergence case here.

Table VI. The increase or decrease in hyperfine frequency from the hyperfine mid-point as a result of the same or opposite sense proton–electron Sp-2 rotation combined with proton motion towards or away from the electron.

proton-electron motion	***same Sp-2 sense***	***opposite Sp-2 sense***
convergence	frequency decrease	frequency increase
divergence	frequency increase	frequency decrease

In the locality of the electron Sp-2, the proton momentum-field vectors $\vec{p}'_{2f}$ are assumed to form a parallel field, see Fig. 4 and Eq. (27). A scalar product of the change in field momentum as the electron Sp-2 circuit moves through the field is to be taken as a line integral around its circuit, averaged over the angle γ, see Fig. 7b.

For a change in distance between the Sp-2 centers $\bar{d}_2$ we give the change in frequency $\Delta\nu_{hf}$ that constitutes the hyperfine shift for the Sp-2 electron circuit in the Sp-2 time period T_2 as follows:

$$\Delta\nu_{hf} = \frac{10^{-6}|\vec{v}_r|\Delta p_2}{h} = \frac{10^{-6}n^2}{h}|\vec{v}_r|\nabla\left(\frac{1}{2\pi}\int_0^{2\pi}\vec{p}'_{2f}\cdot d\hat{r}\right)\cdot\vec{v}_r T_2, \quad \nabla=\begin{pmatrix}\frac{\partial}{\partial x}\\ \frac{\partial}{\partial y}\\ 0\end{pmatrix}, \quad \vec{v}_r=\begin{pmatrix}v_x\\ v_y\\ v_z\end{pmatrix} \tag{25}$$

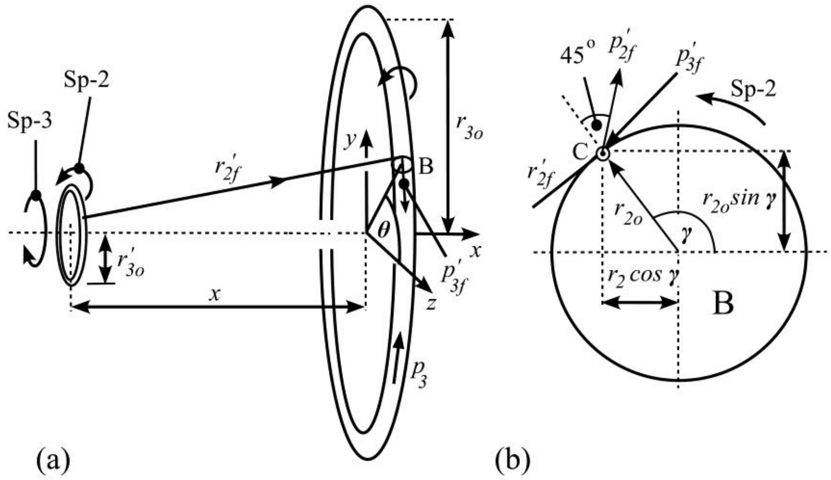

Figure 7. a Proton PTV (left) bound to an electron PTV (right), not to scale. **b** Expanded view of the electron Sp-2 circuit B with the parameters $(x, r_{3o}, r_{2o}, \gamma)$ in $\vec{r}'_{2f}$ describing point C on the circuit, see Eq. (25). In this example, the proton and electron Sp-2 rotations have the same sense. The magnetic field momentum p'_{2f} intersects the fixed line joining the proton-electron Sp-2 centers at 45° (and this line is not r'_{2f} whose direction varies with γ).

---

[18] The ends of the frustrum are the proton and electron toroidal areas, see Fig. 7a.

[19] As Ref. [4, footnote 27] indicates, the electron Sp-2 motion is envisaged as an iterative incremental change along r'_{2f} followed by an incremental restoration of r_{3o}.

Following Ref. [4, Eq. (72) and Fig. (13)], the n^2 in Eq. (25) shows the number of electron Sp-2 circuits that are receptive to the change in proton field momentum. Here, Δp_2 is the total change in the mean magnetic momentum field around the Sp-2 circuits, $\vec{p}'_{2f}$ is the Sp-2 proton field momentum in the locality of the electron, $d\hat{r}$ is the incremental unit tangent vector for the Sp-2 electron radius, and $\vec{v}_r$ is the electron velocity vector along r'_{2f}. Let y be the distance between the proton and electron Sp-2 centers, taken perpendicular to their common toroidal axis, see Fig. 4a, where $y = (r_{3o} - r'_{3o})$. Then we have

$$r'_{2f} = (x + r_{2o}\cos\gamma)^2 + (y + r_{2o}\sin\gamma)^2 \sim (x^2 + y^2 + 2r_{2o}(x\cos\gamma + y\sin\gamma))^{1/2} \tag{26}$$

having ignored powers of $r_{2o} \sim \alpha r_{3o}$ higher than first order [4, Eq. (70)].

The orientation of $\vec{p}'_{2f}$ field vector introduces a geometric projection factor $\cos(\pi/4) = 1/\sqrt{2}$ that reduces the effective field coupling, see Sec. 1.3.5. We represent both the proton and electron Sp-2 circuits rotating counter clockwise in Fig. 7 as

$$\vec{p}'_{2f} = \frac{\hbar}{r'_{2f}} \begin{pmatrix} -\dfrac{y}{\sqrt{2}(x^2+y^2)^{1/2}} \\ \dfrac{x}{\sqrt{2}(x^2+y^2)^{1/2}} \\ 0 \end{pmatrix}, \quad d\hat{r} = \begin{pmatrix} -\sin\gamma \\ \cos\gamma \\ 0 \end{pmatrix} d\gamma \tag{27}$$

Table VII. Correction multipliers k in Eq. (35) for various groups of hyperfine states.

State	$nS_{1/2}$	$nP_{1/2}$	$nP_{3/2}$	$nD_{3/2}$	$nD_{5/2}$
Multiplier k	1	1/3	2/15	2/25	25/486

Table VIII. Results for the magnitude of the hydrogen hyperfine shift from the mid-point hyperfine frequency (MHz) for various states using Eq. (35). Relativistic reduced mass and increased proton speed adjustments are included. The experimental value is at the top [20, Table III], and the PTV value at the bottom. The error magnitude is given as hf-error.

State	Experiment/ PTV model	hf-error	State	Experiment/ PTV model	hf-error
$1S_{1/2}$	710.202 9 710.019 8	0.183 1	$5P_{3/2}$	0.756 9 0.757 3	0.000 4
$2S_{1/2}$	88.778 4 88.748 1	0.030 3	$6P_{3/2}$	0.438 0 0.438 2	0.000 2
$3S_{1/2}$	26.304 7 26.295 1	0.009 6	$7P_{3/2}$	0.275 9 0.276 0	0.000 1
$4S_{1/2}$	11.097 3 11.093 1	0.004 2	$3D_{3/2}$	2.103 3 2.103 5	0.000 2
$5S_{1/2}$	5.681 8 5.579 6	0.002 2	$4D_{3/2}$	0.887 4 0.887 4	0.000 1
$6S_{1/2}$	3.288 0 3.286 8	0.001 3	$5D_{3/2}$	0.454 4 0.454 4	0.000 0
$2P_{1/2}$	29.584 8 29.582 7	0.002 0	$6D_{3/2}$	0.262 9 0.262 9	0.000 0
$3P_{1/2}$	8.765 9 8.765 0	0.000 9	$7D_{3/2}$	0.165 6 0.165 6	0.000 0
$4P_{1/2}$	3.698 1 3.697 7	0.000 4	$8D_{3/2}$	0.110 9 0.110 9	0.000 0
$5P_{1/2}$	1.893 5 1.893 2	0.000 2	$3D_{5/2}$	1.351 7 1.352 6	0.000 9
$6P_{1/2}$	1.095 7 1.095 6	0.000 1	$4D_{5/2}$	0.570 4 0.570 6	0.000 3
$7P_{1/2}$	0.689 8 0.689 9	0.000 2	$5D_{5/2}$	0.292 0 0.292 2	0.000 2
$2P_{3/2}$	11.825 8 11.832 4	0.006 7	$6D_{5/2}$	0.169 0 0.169 0	0.000 1
$3P_{3/2}$	3.504 0 3.505 9	0.001 9	$7D_{5/2}$	0.106 4 0.106 4	0.000 0
$4P_{3/2}$	1.478 3	0.000 8	$8D_{5/2}$	0.071 3	0.000 0

1.479 0	0.071 3

A variation in r'_{2f} controls the strength of the magnetic momentum field $|\vec{p}'_{2f}|$, while its direction vector, being independent of γ, ensures a parallel field in the locality of the electron.

As a result of the motion of the electron through the proton momentum-field, there is a change in the mean momentum Δp_2 around the Sp-2 electron ring during the time it takes to complete one electron Sp-2 circuit T_2. From Eq. (25) and the structure of the Sp-2 circuits — see Ref. [4, Fig. 13, Eq. (72)] — we have

$$\Delta p_2 = \frac{n^2}{2\pi}\int_0^{2\pi}\frac{\partial \vec{p}'_{2f}}{\partial x}\cdot d\hat{r}\; v_x T_2 + \frac{n^2}{2\pi}\int_0^{2\pi}\frac{\partial \vec{p}'_{2f}}{\partial y}\cdot d\hat{r}\; v_y T_2 \tag{28}$$

The magnitude of the velocity vector that represents the displaced momentum out of the electron PTV along r'_{2f} at the state boundary is given by [4, Eq. (50)], thus

$$\vec{v}_r = \begin{pmatrix} v_x \\ v_y \\ v_z \end{pmatrix} = \frac{\alpha c}{\sqrt{2}Y\left(1+\frac{\alpha^2}{Y^2}\right)^{1/2}}\begin{pmatrix} -\frac{x}{(x^2+y^2)^{1/2}} \\ -\frac{y}{(x^2+y^2)^{1/2}} \\ 0 \end{pmatrix} \tag{29}$$

Then from Eq. (27) since

$$\vec{p}'_{2f}\cdot d\hat{r} = \frac{\hbar}{\sqrt{2}}\left(r'_{2f}\right)^{-1}(x^2+y^2)^{-\frac{1}{2}}(y\sin\gamma + x\cos\gamma) \tag{30}$$

to first order in r_{2o} we arrive at the following

$$n^2\int_0^{2\pi}\frac{\partial}{\partial x}\left(\vec{p}'_{2f}\cdot d\hat{r}\right) = -\frac{2\pi n^2\hbar x r_{2o}}{\sqrt{2}\,X^4}, \quad X = (x^2+y^2)^{\frac{1}{2}} \tag{31}$$

Equation (31) arises from same sense Sp-2 rotations and $\partial/\partial x$ taken as positive which means that the electron is receding from the proton. If we reverse the sign of $\partial/\partial x$ so that the proton and electron converge, the sign of Eq. (31) becomes positive, then using Eq. (29) the sign reverses again as in Eq. (32). Here, we should keep in mind that at a state boundary, any additional momentum that is redistributed from the Sp-2 circuit into Sp-3 momentum joins the translational motion of the toroid on its helical trajectory at a rake of $\pi/4$ on the frustrum. Differentiation with respect to y replaces x with y in the numerator of Eq. (31) and use of Eq. (29) gives

$$\Delta\nu_{hf} = -\frac{10^{-6}n^2\alpha c}{\sqrt{2}hY\left(1+\frac{\alpha^2}{Y^2}\right)^{1/2}}\frac{\hbar r_{2o}}{\sqrt{2}\,X^3}\begin{pmatrix} x/X \\ y/X \\ 0 \end{pmatrix}\cdot\begin{pmatrix} x/X \\ y/X \\ 0 \end{pmatrix}\frac{\alpha c}{\sqrt{2}Y\left(1+\frac{\alpha^2}{Y^2}\right)^{\frac{1}{2}}}\frac{2\pi r_{2o}\left(1+\frac{\alpha^2}{Y^2}\right)^{1/2}}{c} \tag{32}$$

having used Eq. (16) when introducing T_2. A conversion from Joules to MHz has also been made using $10^{-6}/h$. Substituting primed (proton) variables for un-primed (electron) we also have [4, Eqs. (63) and (70)]

$$r_{2o} = \frac{\alpha}{(1-\alpha^2)^{1/2}}r_{3o}, \quad \hbar = \frac{m_o\alpha c r_{3o}}{(1-\alpha^2)^{1/2}}, \quad r'_{3o} = \frac{m_o}{m'_o}\,r_{3o} = Mr_{3o} \tag{33}$$

Noting that

$$y = r_{3o} - r'_{3o}, \quad \frac{dy}{dr_{3o}} = 1 \tag{34}$$

Then using Eq. (33), the Rydberg frequency Ry from Table XVIII (see associated footnote), and normalizing the length X to $\bar{d}_2$ with a division by r_{3o} gives

$$\Delta\nu_{hf} = -\frac{2\pi n^2\alpha^3 Ry}{\sqrt{2}\,Y^2\left(1+\frac{\alpha^2}{Y^2}\right)^{1/2}\bar{d}_2^3(1-\alpha^2)^{3/2}}, \quad \bar{d}_2 = (\bar{x}^2+(1-M)^2)^{\frac{1}{2}} \sim 2n \tag{35}$$

Here, $\bar{d}_2$ is the normalised bound-state distance between the proton–electron Sp-2 centers [4, Table 2]. So since $Y\sim n$ then $\Delta\nu_{hf} \propto n^{-3}$. The negative sign of Eq. (35) represents the case in which the proton and electron are converging (x decreasing) and their Sp-2 rotation senses are the same, see Table VI.[20] The PTV model results for Eq. (35) can be positive or negative and their magnitudes are shown against the experimental values in Table VIII for the half-splitting.[21]

The multipliers k obtained by data-fitting are listed in Table VII and produce good agreement with experiment. We note that $k = 1$ gives accurate values for the $nS_{1/2}$ states, meaning that these states need no adjustment, thus supporting the parallel field assumption.[22] The values for $\Gamma > 0$ in Eq. (13) represent the proton moving towards the electron in the center of mass frame, see Table I.

4. PTV and QED errors

4.1. Lamb shift

Table IX. Comparison of the QED [18, Table 4 end column] and PTV Lamb shift absolute errors for 16 states of hydrogen from Tables IV and V.The $1S_{1/2}$ error is given by Ref. [18, p.600]. All frequencies are in MHz.

State	QED error	PTV error ($\Gamma > 0$)	PTV error ($\Gamma < 0$)
$1S_{1/2}$	0.3	0.000 0	0.000 0
$2P_{1/2}$	0.002	0.000 0	0.000 0
$2S_{1/2}$	0.000 03	0.000 0	0.000 0
$2P_{3/2}$	0.003	0.000 0	0.000 0
$3P_{1/2}$	0.64	0.000 0	0.000 0
$3S_{1/2}$	0.7	0.000 0	0.000 0
$3D_{3/2}$	0.6	0.000 0	0.000 0
$3P_{3/2}$	0.64	0.000 0	0.000 0
$3D_{5/2}$	0.76	0.000 0	0.000 0
$4P_{1/2}$	0.018	0.000 0	0.000 0
$4S_{1/2}$	0.007	0.095 8	0.008 9
$4D_{3/2}$	0.26	0.000 0	0.000 0
$4P_{3/2}$	0.01	0.000 0	0.000 0
$4D_{5/2}$	0.016	0.000 0	0.000 0
$5P_{1/2}$	0.1	0.002 9	0.000 9
$5S_{1/2}$	0.1	0.119 4	0.014 1

For the QED calculations, the centroids of the hyperfine levels of atomic hydrogen are given by Ref. [18, p.600, Table 4] relative to the $1S_{1/2}$ state or ionization limit *3 288 086 856.8(7)* MHz. The error ΔE_{exp-th} (MHz) between the experimentally determined values and the QED calculations which are listed as 'QED error' in Table IX are also given in Ref. [18, Table 4]. The QED error for the $1S_{1/2}$ state of *0.3* MHz is discussed in Ref. [18, p.600 second column]. The PTV theory does not aim for the centroid but the mid-point value of the two hyperfine frequencies as calculated from values given by Ref. [20, Tables III, IV, and V]. The empirically determined Eqs. (12), (13), and (22) are used to achieve this. The PTV Lamb shift for the ground state is ~ 450 times greater than the tra-

---

[20] Note that an increasing (positive) ∂x in Eq. (31) corresponds to electron motion away from the proton.

[21] The experimental hyperfine mid-point is calculated from half the difference between the upper and lower hyperfine values [20, Table III].

[22] If the reduced mass and D-function are introduced into Eq. (35) there is 1.1 MHz error for $1S_{1/2}$ when $\Gamma > 0$.

ditional Lamb shift frequency.[23] So it is important to note that Table IX is not a *direct* comparison, as the QED and PTV Lamb shifts are different intervals. The absolute errors between experiment and PTV theory for this shift, taken from Tables IV and V. The PTV mean absolute error is 0.0076 MHz against the QED mean absolute of 0.2598 MHz.

4.2. Hyperfine shift

While the QED calculation for the hyperfine splitting employs unequal displacements about the centroid — see Eq. (4) — the PTV calculation uses an equal displacement above and below the mid-point of the two hyperfine levels, Eq. (35). Table X shows the magnitude of the hyperfine shift in which all experimental values in the second column are taken from Ref. [20, Tables III, IV, and V] in MHz. The QED calculations for the $nS_{1/2}$ states in the third column are given by Ref. [22, Table 3], except the $1S_{1/2}$ state which is provided by Ref. [23, p.39]. For the non-$nS_{1/2}$ states, the QED values are taken from Ref. [18, Table 1]. All experimental values have been converted to a half-splitting for comparison with the PTV values. The PTV mean absolute error is 0.0152 MHz (median 0.0014 MHz)against the QED value of 0.0003 MHz. Taken over 30 states, the PTV value is 0.0082 MHz. All errors are given to the nearest 0.1 kHz.

Table X. Comparison of the QED and PTV hydrogen hyperfine splitting absolute errors from Table VIII. All values are in MHz.

State	Experiment	QED calc.	PTV calc.	QED error	PTV error
$1S_{1/2}$	710.202 9	710.202 9	710.019 8	0.000 0	0.183 1
$2P_{1/2}$	29.584 7	29.584 7	29.582 7	0.000 0	0.002 0
$2S_{1/2}$	88.778 4	88.778 4	88.748 1	0.000 0	0.030 3
$2P_{3/2}$	11.825 8	11.825 8	11.832 5	0.000 0	0.006 7
$3P_{1/2}$	8.765 9	8.764 0	8.765 0	0.001 9	0.000 9
$3S_{1/2}$	26.304 7	26.304 7	26.295 1	0.000 0	0.009 6
$3D_{3/2}$	2.103 3	2.102 5	2.103 5	0.000 8	0.000 2
$3P_{3/2}$	3.503 9	3.504 0	3.505 9	0.000 1	0.001 9
$3D_{5/2}$	1.351 7	1.351 7	1.352 6	0.000 0	0.000 9
$4P_{1/2}$	3.698 1	3.698 1	3.697 7	0.000 0	0.000 4
$4S_{1/2}$	11.097 3	11.097 3	11.093 1	0.000 0	0.004 2
$4D_{3/2}$	0.887 4	0.887 0	0.887 4	0.000 4	0.000 1
$4P_{3/2}$	1.478 2	1.478 2	1.4789 0	0.000 0	0.000 8
$4D_{5/2}$	0.570 3	0.570 7	0.570 6	0.000 4	0.000 3
$5P_{1/2}$	1.893 4	1.893 0	1.893 2	0.000 4	0.000 2
$5S_{1/2}$	5.681 8	5.681 8	5.679 6	0.000 0	0.002 2

5. Extension to other isotopes

5.1. Deuterium validation

We now replace $\hbar$ with $Z_e\hbar$ in Ref. [4, first of Eq. (35)] where $Z_e \in \mathbb{Z}^+$. This is the electron self-potential angular momentum. Also, we allow the nuclear Sp-3 angular momentum $\hbar$ to become $Z_n\hbar$ in Ref. [4, Eq.(74)] where $Z_n \in \mathbb{Z}^+$. This affects the nuclear Sp-3 field. For deuterium, we replace the proton mass m'_o with $2m'_o$, and similar to hydrogen $Z_e = 1$ and $Z_n = 1$.[24] As with hydrogen, a search is conducted for Γ in Eqs (12) and (13) that yields the most consistent B values using Eq. (23). We then search through the A in Eq. (22) to minimize $\Delta\nu_{err}$ in Eq. (24). The values of A, B, Γ, and A/Γ for deuterium are given in Tables XI and XII. Unlike hydrogen, $\Delta\nu_{err}$ does not minimize to zero

---

[23] For example, for the $1S_{1/2}$ state, the QED Lamb shift is $\sim 8 \times 10^3$ MHz against the PTV shift of $\sim 3.6 \times 10^6$ MHz ($\Gamma > 0$).

[24] This is intentionally chosen to be integer. The atomic mass 2.01355 amu produces greater errors.

which suggests that a more intricate mechanism for the nucleus is at work than that for Eq. (22) with hydrogen. However, the minima produced for $\Gamma > 0$ give a mean absolute error of *2.651* MHz (see Table XIII), and for $\Gamma < 0$ a mean absolute error of *3.6291* MHz, with the same 18 states tested in each case.

Table XI. The optimized radiation exit shift constants (A, B) in Eq. (22) for 18 states of deuterium $nS_{1/2}$ $(n = 1,2,\ldots,6)$, $nP_{1/2}$ $(n = 2,3,\ldots,7)$, and $nP_{3/2}$ $(n = 2,3,\ldots,7)$, for $\Gamma > 0$ in Eqs. (13) and (22).

States	A (MHz)	B	Γ	A/Γ (MHz)
$nS_{1/2}$	−30 569 665.185	−2.999 892 049 26	2.127 91	−14 366 052
$nP_{1/2}$	−53 763 040.95	−3.000 001 594 73	3.749 99	−14 336 849
$nP_{3/2}$	−58 343 368.475	−3.000 044 76 37	4.069	−14 338 503

Table XII. The optimized radiation exit shift constants (A, B) in Eq. (22) for 18 states of deuterium $nS_{1/2}$ $(n = 1,2,\ldots,6)$, $nP_{1/2}$ $(n = 2,3,\ldots,7)$, and $nP_{3/2}$ $(n = 2,3,\ldots,7)$, for $\Gamma < 0$ in Eqs. (13) and (22).

States	A (MHz)	B	Γ	A/Γ (MHz)
$nS_{1/2}$	30 575 683.063	−2.999 964 102 157	−2.139 01	−14 294 315
$nP_{1/2}$	53 953 268	−2.999 932 389 964	−3.766 4	−14 324 891
$nP_{3/2}$	58 285 890.96	−2.999 912 760 85	−4.069 08	−14 324 096

Table XIII. Deuterium hyperfine mid-point results for the red shift $\Gamma > 0$ (Table XI), with the $nS_{1/2}$ states $(n = 1,2,\ldots,6)$, $nP_{1/2}$ states $(n = 2,3,\ldots,7)$, and $nP_{3/2}$ states $(n = 2,3,\ldots,7)$. The experimental mid-point hyperfine values ν_{exp} [18, Tables 6] are the top values, and the optimized values given by Eqs. (12), (13), and (22) are the lower values.

State	$\boldsymbol{\nu_{exp}}$ (MHz) $(\boldsymbol{\nu_{3D}} - \Delta\boldsymbol{\nu_{shift}})$	$\Delta\boldsymbol{\nu_{err}}$ (MHz)	State	$\boldsymbol{\nu_{exp}}$ (MHz) $(\boldsymbol{\nu_{3D}} - \Delta\boldsymbol{\nu_{shift}})$	$\Delta\boldsymbol{\nu_{err}}$ (MHz)
$1S_{1/2}$	3 288 981 575.664 1 3 288 981 575.664 1	0.000 1	$5P_{1/2}$	131 559 030.725 4 131 559 031.988 0	1.262 6
$2S_{1/2}$	822 249 120.399 0 822 249 120.399 0	0.000 1	$6P_{1/2}$	91 360 319.854 1 91 360 322.368 2	2.514 0
$3S_{1/2}$	365 442 988.521 0 365 442 996.621 6	8.100 6	$7P_{1/2}$	67 121 801.153 0 67 121 804.785 5	3.632 5
$4S_{1/2}$	205 561 211.283 9 205 561 219.063 8	7.779 9	$2P_{3/2}$	822 239 201.674 9 822 239 201.674 9	0.000 0
$5S_{1/2}$	131 558 962.536 5 131 558 966.448 5	3.911 9	$3P_{3/2}$	365 440 051.200 0 365 440 051.200 0	0.000 0
$6S_{1/2}$	91 360 280.352 6 91 360 284.413 2	4.060 5	$4P_{3/2}$	205 559 971.904 3 205 559 976.033 3	4.129 0
$2P_{1/2}$	822 250 175.132 2 822 250 175.132 2	0.000 0	$5P_{3/2}$	131 558 328.313 2 131 558 330.178 1	1.864 9
$3P_{1/2}$	365 443 302.533 3 365 443 302.533 3	0.000 0	$6P_{3/2}$	91 359 913.355 0 91 359 916.376 8	3.021 9
$4P_{1/2}$	205 561 343.854 0 205 561 347.251 1	3.407 0	$7P_{3/2}$	67 121 545.165 7 67 121 549.206 3	4.040 6

From Tables XI and XII, the mean value of $A/\Gamma = -14{,}330{,}784$ taken across the six sets of states. The experimental hyperfine mid-points in Table XIII are calculated from the centroids in Ref. [20, Table 6] taking into account the $2:1$ ratio of the splitting about the centroid.

The hyperfine shifts are shown in Table XIV. For deuterium, Eq. (35) now needs an extra universal multiplier of *0.2305458* which applies across all deuterium states, and $k = 1/15$ for $nP_{3/2}$ in Table VII. This suggests that the Sp-2 magnetic momentum field of the deuterium nucleus has a smaller effect than that of hydrogen which needs no universal multiplier. The mean value of the absolute errors hf-error in Table XIV is *0.0017* MHz.

Table XIV. Results for the deuterium hyperfine shift from the mid-point hyperfine frequency (MHz) for various states using Eq. (35). The experimental value is at the top [18, Table 2], and the PTV value at the bottom. The error magnitude is given as hf-error.

State	Experiment/ PTV model	hf-error	State	Experiment/ PTV model	hf-error
$1S_{1/2}$	163.692 1 163.692 1	0.000 0	$5P_{1/2}$	0.436 3 0.436 5	0.000 2
$2S_{1/2}$	20.462 2 20.460 5	0.001 7	$6P_{1/2}$	0.252 5 0.252 6	0.000 1
$3S_{1/2}$	6.062 9 6.062 2	0.000 7	$7P_{1/2}$	0.159 0 0.159 1	0.000 1
$4S_{1/2}$	2.557 8 2.557 5	0.000 3	$2P_{3/2}$	1.349 7 1.364 0	0.014 2
$5S_{1/2}$	1.309 6 1.309 4	0.000 2	$3P_{3/2}$	0.399 9 0.404 1	0.004 2
$6S_{1/2}$	0.757 8 0.757 8	0.000 0	$4P_{3/2}$	0.168 7 0.170 5	0.001 8
$2P_{1/2}$	6.816 7 6.820 2	0.003 5	$5P_{3/2}$	0.086 4 0.087 3	0.000 9
$3P_{1/2}$	2.019 8 2.020 7	0.000 9	$6P_{3/2}$	0.050 0 0.050 5	0.000 5
$4P_{1/2}$	0.852 1 0.852 5	0.000 4	$7P_{3/2}$	0.031 5 0.031 8	0.000 3

5.2. Nuclear mass number scaling

Data for only three $nS_{1/2}$ states has been found for tritium [18, Table 8] and an investigation shows that similar to deuterium, the gradient difference $\left(B_{n+1,n+2} - B_{n,n+1}\right)$ in Eq. (23) does not minimize as effectively as for hydrogen but nevertheless exhibits non-zero minima for both $\Gamma > 0$ and $\Gamma < 0$. The proton mass m_o' now becomes $3m_o'$. Here, $Z_e = 1$ and $Z_n = 1$, the same values as those for hydrogen and deuterium. This data is shown in Table 15.

Table XV. The optimized radiation exit shift constants (A, B) in Eq. (22) for 3 states of tritium $nS_{1/2}$ for both signs of Γ in Eqs. (13) and (22).

States	A (MHz)	B	Γ	A/Γ (MHz)
$nS_{1/2}$	−232 046 281.804	−3.001 439 588	24.201	−9 588 293
$nS_{1/2}$	229 508 392.686	−2.998 419 199	−24.107	−9 520 405

The mean value of $A/\Gamma = -9{,}554{,}349$ MHz. This brings us to a nuclear scaling law for hydrogen, deuterium, and tritium in which

$$\frac{A}{\Gamma} = -\frac{28{,}651{,}713}{A_n} \tag{36}$$

where A_n is the nuclear mass number.

5.3. Nuclear charge effects

We now investigate the value of A/Γ for $^3\mathrm{He}^+$ which consists of two protons and one neutron ($3m_o'$), but carries a nuclear charge of $Z_n = +2$. This is the number we associate with the unloaded PTV self-potential angular momentum in Ref. [4, first of Eq. (35)] in which $\hbar$ becomes $Z_n\hbar$. We also set $Z_e = 2$ which means that every α in Eq. (12) is replaced by $Z_e\alpha$. These values produce the smallest difference in gradients using Eq. (23) when obtaining B and both must appear in the optimization search Ref. [4, Eq. (85)], to find the bound-state distance $\bar{d}_2$ in Ref. [4, Eq. (86)]. Table XVI shows the results of the investigation for the $nS_{1/2}$ states.

Table XVI. The optimized radiation exit shift constants (A, B) in Eq. (22) for 3 states of ^{3}He$^+$ $nS_{1/2}$ for both signs of Γ in Eqs. (13) and (22).

States	A (MHz)	B	Γ	A/Γ (MHz)
$nS_{1/2}$	−293 835 287.1137	−3.007 805 556	61.25	−4 797 311
$nS_{1/2}$	287 323 833.1421	−2.992 097 643	−60.385	−4 758 199

The mean value of $\mathrm{A}/\Gamma = -4{,}777{,}755$ MHz. A preliminary investigation for ^{7}Li^{2+} $(A_n = 7)$ on the $nS_{1/2}$ states using $\Gamma > 0$ and has shown that for $Z_e = 3,\ Z_n = 3$, and $7m'_o$ we have $\mathrm{A}/\Gamma = -1{,}364{,}437$. With $\Gamma < 0$ we obtain $\mathrm{A}/\Gamma = -1{,}366{,}328$. Their mean value is shown in Table XVII.

5.4. *Universal nuclear scaling law*

We now suggest a scaling law for nuclei relative to the mean-value hydrogen result as follows:

$$\frac{A}{\Gamma} = -\frac{28{,}651{,}713}{A_n Z_n} \tag{37}$$

where Z_n is the nuclear charge which in the PTV model is the nuclear Sp-3 angular momentum $Z_n\hbar$. The Z_e appears in the internal-potential term in Ref. [4, Eqs. (31) and (35)] so that the $\hbar$ or α is replaced with $Z_e\hbar$ or $Z_e\alpha$, respectively. The accuracy of Eq. (37) is summarized in Table XVII.

Table XVII. Comparison of theory with PTV model for the universal scaling law applied to hydrogen, deuterium, tritium, ^{3}He$^+$, and ^{7}Li^{2+}. The PTV prediction for A/Γ modelled on experiment is compared with the theoretical values from Eq. (37).

Element	A_n	Z_n	Z_e	PTV (MHz)	Eq. (37) (MHz)	% error magnitude
H	1	1	1	−28 651 713	−28,651,713	0
D	2	1	1	−14 330 784	−14 325 857	0.03
T	3	1	1	−9 554 349	−9 550 571	0.04
$^3He^+$	3	2	2	−4 777 755	−4 775 286	0.05
$^7Li^{2+}$	7	3	3	−1 365 383	−1 364 367	0.01

6. Conclusions

6.1. *Physical interpretation*

The strength of the PTV model lies in its development of a visualizable mechanism for atomic spectra and the accuracy achieved suggests that geometrical approaches merit further attention. This architecture represents electrons and protons as helical string-like structures in optical OAM (Sp-2) with trajectories that are diverted into a toroidal structure (Sp-3). The Sp-2 and Sp-3 rotations are responsible for magnetic and electric effects, respectively. Within the model, interactions become exchanges of geometric momentum: the proton's Sp-3 field occupies the electron PTV and displaces one half of its rotational energy into emissible translational energy to form a bound state. The hyperfine interaction is represented as a change in the proton Sp-2 field integrated around the electron Sp-2 circuit.

The observed field-free quantization of electron vortex beams [6–8], in which high-integer angular momenta can be generated without an external potential, suggest that non-vortex-beam electrons might also have this property. PTV theory introduces an effective internal potential that allows quantized states to occur without explicit reliance on the Coulomb potential on which the Sommerfeld–Dirac theories depend. In bound-state systems between PTVs of vastly different mass such as hydrogen ($M \ll 1$), the more massive PTV effectively defines the reference frame for the measurement of radiation emissions. While both Sp-3 fields displace the other's Sp-3 momentum into translational motion, only the lighter PTV's emission contributes to the observed spectral line. The more massive PTV continues its translational motion (induced by the lighter PTV's Sp-3 field) while the electron's motion is taken relative to the proton field in its Sp-3 rotation through the introduction of the reduced mass. Transitions arise as differences between Sp-3 rotational frequencies, and the occurrence of emission or absorption depends on the relative rotation senses of the incident radiation and the target Sp-3 level.

PTV applies the same three state-independent calculations to all 60 hydrogen states tested: 30 states with $\Gamma > 0$ (red shifts) and $\Gamma < 0$ (blue shifts). These calculations are the modified fine-structure Eq. (12), magnetic potential adjustment Eq. (22), and the hyperfine shift Eq. (35). The parameters Γ, A, B, and k exhibit systematic behaviour: Γ and A are connected by a universal scaling law Eq. (37) that applies across hydrogen, deuterium, tritium, $^3He^+$, and $^7Li^{2+}$; in Eq. (22), $B \sim -3.000$ across all states tested; and in Eq. (35), $k = 1$ for all hydrogen $nS_{1/2}$ states is a *prediction* that supports the parallel-field approximation. A preliminary investigation shows that varying the eccentricity of the electron Sp-2 circuits while maintaining a constant perimeter can appropriately reduce the receptivity of these circuits to the varying proton Sp-2 field, and account for the various k in Table VII. These patterns in the parameters address the objection of 'curve fitting' by providing evidence of an underlying geometrical structure to atomic processes.

Deuterium supports the model's extension to composite nuclei: absolute hyperfine mid-point frequencies achieve 22 parts per billion accuracy (Table XIII: 8 MHz error at 3.7×10^8 MHz for $3S_{1/2}$ and $\Gamma > 0$), while hyperfine shifts show at most $\sim 1\%$ error. This demonstrates that energy-balance and Sp-2 principles can be suitably approximated by the hydrogen PTV model for systems with light nuclei.

The universal scaling of the D-function parameter Γ with the magnetic potential parameter A with nuclear mass number A_n reflects an inherent reciprocity: a spatial differentiation of the Sp-2 momentum field followed by integration over the spatial trajectory from infinity to the bound-state displacement, yielding an endpoint-defined interaction energy. Within the Sp-2 framework, Sp-2 momentum fields are reciprocal, so this operation applies equally to electron and nuclear vortices. The apparent static character of the resulting interaction reflects the cancellation of the spatial differentiation by the spatial integration rather than the absence of underlying dynamics.

The PTV approach demonstrates that computational simplicity need not imply conceptual simplicity. While individual calculations remain calculator-executable (see Appendix B), their mutual consistency across fine structure, Lamb shift, and hyperfine splitting requires careful geometric coordination. This architectural coherence — where parameters determined for one phenomenon constrain predictions for others — provides internal validation absent in purely phenomenological models.

6.2. Future developments

The construction of more complex nuclei than hydrogen from PTVs is a task for future research. For hydrogen, two oppositely rotating Sp-3 vortices of different scale can bind, and the electron forms its bound state at the point when the nuclear Sp-3 momentum field has displaced half of the electron Sp-3 momentum into translational motion. This energy-balance condition [4, Eq. (85)] ensures that exactly half of the original electron Sp-3 energy radiates away. The half that is left in the electron produces a Sp-3 momentum field that displaces the same momentum out of the proton into translational motion. So both PTVs lose the same momentum which is that of the smaller PTV. The question is whether or not this can be applied to the construction of light nuclei. What needs to be investigated is whether or not a neutron might be composed from two proton-scale PTVs with opposite Sp-3 that possess $Z_n = +1$ (clockwise) and $Z_n = -1$ (counter clockwise).

At the binding distance $\bar{d}_2$, each radiates away one half of its Sp-3 energy leaving $Z_n = 1/2$ and $Z_n = -1/2$. These two oppositely rotating Sp-3 angular momenta cancel out to zero charge, while the Sp-2 angular momenta reinforce. This assumes that the Sp-2 and Sp-3 angular momenta are equal. This would be exactly the same physical process as hydrogen formation but at nuclear scale. Whether PTV ultimately explains nuclear binding energies on this basis or reveals limitations in geometric approaches, the present work demonstrates that visualization and formalism can coexist productively as complementary approaches.

Appendix

Appendix A: CODATA constants

Table XVIII shows the values of the constants used in the new PVT calculations. In the following notation, primed variables refer to the proton and unprimed variables to the electron.

Table XVIII. 2018 CODATA values for constants used [24].

symbol	constant	CODATA value
α	Fine structure constant	0.007 297 352 569 3
c	Speed of light in vacuum	299 792 458 (ms^{-1})
g_p	Landé g-factor for proton	5.585 694 689
m_o	Rest mass electron	$9.109\,383\,701\,5 \times 10^{-31}$ (kg)
m_o'	Rest mass proton	$1.672\,621\,923\,695 \times 10^{-27}$ (kg)
M	Rest mass electron/proton	0.000 544 617 021 488
h	Planck's constant	$6.626\,070\,15 \times 10^{-34}$ $(J\,Hz^{-1})$
Ry	Rydberg frequency[25]	3 289 841 960.250 86 (MHz)
π	pi	3.141 592 653 589 793

Appendix B: Example calculation for the $2S_{1/2}$ *state* ($\Gamma > 0$)

This is the calculation represented in Fig. 5. Here $n_r = 1$, $n_\phi = 1$. In general, we choose the appropriate (n_r, n_ϕ), obtain the radiation exit-shift constants from Table II, the hyperfine-splitting multipliers from Table VII, and the bound state separation distances from Ref. [4, Table 2]. The equations are then exactly the same as the following.

This example demonstrates the calculation for states where $n_\phi = 1$, requiring no empirical correction to the hyperfine splitting ($k = 1$ in Table VII) which supports the parallel field approximation. All energies have been converted to frequencies (MHz) by multiplying by $10^{-6}/h$. The CODATA constants used are given in Table IX.

STEP 1: Unadjusted fine structure calculation

The equation for this is obtained from Ref. [4, Eq. (51)] converted to frequency (MHz) by multiplying by $10^{-6}/h$.

$$n = n_r + n_\phi = 2, \qquad Y = n_r + \left(n_\phi^2 - \alpha^2\right)^{1/2} = 1.999973374 \tag{38}$$

Noting that $Ry = 0.5 \times m_o \alpha^2 c^2 \times 10^{-6}/h$ we have[26]

---

[25] Calculated from $Ry = 0.5 \times m_o \alpha^2 c^2 \times 10^{-6}/h$.

[26] Using the CODATA constants we find that $0.5 \times m_o \alpha^2 c^2 \times 10^{-6}/h = 3{,}289{,}841{,}960.2445$ against $Ry = 3{,}289{,}841{,}960.2508$. So there is a difference in the second decimal place. The value of Ry is used in the fine structure calculation but the components are used in the hyperfine splitting as the discrepancy there is negligible.

https://doi.org/10.3390/xxxxx

$$\nu_3 = Ry \times \frac{1}{Y^2\left(1+\frac{\alpha^2}{Y^2}\right)} \times \frac{1}{\sqrt{1-\frac{\alpha^2}{2Y^2\left(1+\frac{\alpha^2}{Y^2}\right)}}} \tag{39}$$

$$= 3{,}289{,}841{,}960.2508 \times 0.2500033283 \times 1.00000332827$$
$$= 822{,}474{,}177.0455 \text{ MHz}$$

STEP 2: Relativistic reduced mass adjustment

This is a calculation for the reduced electron rest mass which will be adjusted in Step 3. From Ref. [4, Eq. (88)] the electron rest mass m_2 (consisting of Sp-2 rest mass m_o and Sp-3 constituents) is

$$m_2 = \frac{m_o}{\sqrt{1-\frac{\alpha^2}{2Y^2\left(1+\frac{\alpha^2}{Y^2}\right)}}} \tag{40}$$

Then the reduced mass becomes

$$\mu = \frac{m_2}{1+\frac{m_2}{m_o'}} = 0.9994556776141 m_2 \tag{41}$$

So using the result from Step 1, the frequency in Eq. (39) after replacing m_o in Ry by Eq. (41) becomes

$$\begin{aligned} \nu_{3r} &= 0.9994556776 \times 822{,}474{,}177.0455 \\ &= 822{,}026{,}485.9391 \text{ MHz} \end{aligned} \tag{42}$$

STEP 3: Relative-to-proton speed adjustment

This is part of the Lamb shift calculation that targets the mid-point of the hyperfine pair. Here, we shall use $n = 2$ and the D-function in Eq. (13). We note that $M = m_o/m_o'$. From Table II, we have $\Gamma = 1.006\,942\,7$ for the $2S_{1/2}$ state, so

$$D(n_r, n_\phi, \Gamma) = \left(1+\frac{\Gamma M}{n}\right)^2 = 1.0005484733 \tag{43}$$

The value in Eq. (43) now multiplies each occurrence of α^2 in Eq. (39) so that the Y is modified to

$$Y_D = n_r + \left(n_\phi^2 - D\alpha^2\right)^{1/2} = 1.99997335936 \tag{44}$$

The relativistic mass is now

$$m_{2D} = \frac{m_o}{\sqrt{1-\frac{D\alpha^2}{2Y^2\left(1+\frac{D\alpha^2}{Y^2}\right)}}} = 1.00000333 m_o \tag{45}$$

Then the updated reduced mass from Eq. (41) becomes

$$\mu = \frac{m_o}{1+\frac{m_{2D}}{m_o'}} = 0.9994556776131 m_o \tag{46}$$

Equation (39) must now be modified keeping in mind that Ry also contains α^2 so it needs D modification, so that

$$\nu_{3rD} = \frac{\mu}{m_2} \times DRy \times \frac{1}{Y_D^2\left(1+\frac{D\alpha^2}{Y_D^2}\right)} \times \frac{1}{\sqrt{1-\frac{D\alpha^2}{2Y_D^2\left(1+\frac{D\alpha^2}{Y_D^2}\right)}}} \quad (47)$$

$$= 0.9994556776131 \times 3{,}291{,}646{,}350.7904 \times 0.25000333012 \times 1.00000333$$

$$= 822{,}477{,}353.0407 \text{ MHz}$$

STEP 4: Magnetic potential red shift

Obtaining the A and B constants from Eq. (22), Table II, and $\overline{d}_2$ from Ref. [4, Table 2] we have

$$\Delta\nu_{shift} = A\bar{d}_2^B = 28{,}923{,}705.16563 \times (4.0001231495)^{-3.0000421859595} \quad (48)$$

$$= 451{,}864.7269 \text{ MHz}$$

So, from Eqs. (47) and (48), the hyperfine mid-point is now

$$\Delta\nu_{mid} = \nu_{3D} - \Delta\nu_{shift}$$

$$= 822{,}477{,}353.0407 - 451{,}864.7269 \quad (49)$$

$$= 822{,}025{,}488.3138 \text{ MHz}$$

This result is shown in Table IV.

STEP 5: Hyperfine red shift

Using Eq. (35), there is now a hyperfine red shift from the hyperfine mid-point calculated in Eq. (49).[27] We have $n = 2,\ k = 1$ from Table VII, and $\overline{d}_2 = 4.0001231495$ from Ref. [4, Table 2]. Here, Ry is the Rydberg frequency, see Table XVIII.

$$\Delta\nu_{hf} = \frac{2\pi n^2\alpha^3 Ry}{\sqrt{2}\,Y^2\left(1+\frac{\alpha^2}{Y^2}\right)^{1/2}\bar{d}_2^3(1-\alpha^2)^{3/2}} = \frac{U_1}{U_2} \quad (50)$$

So

$$U_1 = 2\pi(2)^2(0.0072973525693)^3(3{,}289{,}841{,}960.2509)$$

$$= 32{,}130.0117 \quad (51)$$

$$U_2 = \sqrt{2}(1.99997335947)^2(1.000013313)^{\frac{1}{2}}(4.0001231495)^3(0.9999467486)^{\frac{3}{2}}$$

$$= 362.0360$$

Then

$$\Delta\nu_{hf} = \frac{U_1}{U_2} = \frac{32{,}130.0117}{362.0360} \quad (52)$$

$$= 88.7481 \text{ MHz}$$

This is shown in Table X. The experimental half-splitting value from Table X is as follows:

$$\Delta\nu_{sep\_exp} = 88.7784 \text{ MHz} \quad (53)$$

STEP 6: The hyperfine level

Combining these calculations involving red shifts we have

$$\Delta\nu_{final} = \nu_{3D} - \Delta\nu_{shift} - \Delta\nu_{hf}$$

$$= 822{,}477{,}353.0407 - 451{,}864.7269 - 88.7481 \text{ MHz} \quad (54)$$

Then our calculated value is

---

[27] This is a half-splitting on one side of the hyperfine mid-point. The $\Gamma < 0$ case gives the blue shift on the other side.

$$\Delta\nu_{hf\_PTV} = 822{,}025{,}399.5657 \quad (F = 1) \tag{55}$$

This can be compared against the following experimental value [20, Table III]:

$$\Delta\nu_{hf\_exp} = 822{,}025{,}399.5354 \quad (F = 1) \tag{56}$$

The accuracy is better than 4 parts in 100 billion.

Conflicts of Interest: On behalf of all authors, the corresponding author states that there is no conflict of interest.

Data Availability Statement: The hyperfine calculation for Eq. (32), a Liberty BASIC computer program, and the data output for that program can be obtained at the following link: https://barryis-puzzled.com/hyperfine

References

1. V. Simulik and I. Krivsky, Lamb shift in classical electrodynamical model of atom, Third International Congress on Geometry, Integrability and Quantization June 14–23, 2001, Vama Bulgaria. I. M. Mladenov and G. L. Naber, editors, Coral Press, Sofia, 2001, pp. 410–430.
2. V. Simulik and I. Y. Krivsky, Relationship between the Maxwell and Dirac equations: symmetries, quantization, models of atom, Reports on mathematical physics **50** (2002): 315–328.
3. S. C. Verrall, M. Atkins, A. Kaminsky, E. Friederick, A. Otto, K. S. Verall, and P. Lynch, Ground state quantum vortex proton model, Foundations of Physics **53**, 28 (2023).
4. B. R. Clarke, A photonic toroidal model of the hydrogen atom fine structure, Quantum Studies: Mathematics and Foundations **12**, 19 (2025) DOI: 10.1007/s40509-025-00364-9
5. C. Wan, Q. Cao, J. Chen, A. Chong, and Q. Zhan, Toroidal vortices of light. Nat. Photon. **16**, 519–522 (2022). https://doi.org/10.1038/s41566-022-01013-y. (Supplementary information Fig. S5a)
6. B. J. McMorran, A. Agrawal, I. M. Anderson, A. A. Herzing, H. J. Lezec, J. J. McClelland, and J. Unguris, Electron vortex beams with high quanta of orbital angular momentum, Science **331** (2011): 192–95, p.194.
7. M. Uchida and A. Tonomura, Generation of electron beams carrying orbital angular momentum, Nature **464** (2010): 737–739.
8. J. Verbeeck, H. Tian, and P. Schattschneider, Production and application of electron vortex beams Nature, **467** (2010): 301–304.
9. C. G. Darwin, The wave equations for the electron, Proceedings of the Royal Society of London A**118** (1928): 654–680.
10. P. A. M. Dirac, The quantum theory of the electron, Proceedings of the Royal Society of London A **117** (1928): 610–624.
11. A. Sommerfeld, Zur quantentheorie de spektrallinien, Annalen der Physik, **51** (1916): 125–167.
12. A. Sommerfeld, Atomic Structure and Spectral Lines, translated into English by Henry Brose (Methuen & Co., 1923), pp.473, 551–52, Appendix A.
13. J. Leach, S. Keen, M. J. Padgett, C. Saunter, and G. D. Love, Direct measurement of the skew angle of the Poynting vector in a helically phased beam, Optics Express **14** (2006): 11919–11924.
14. W. E. Lamb and R. C. Retherford, Fine structure of the hydrogen atom, Physical Review **72**, 3 (1947): 241–243.
15. H. A. Bethe, L. M. Brown, and J. R. Stehn, Numerical value of the Lamb shift, Physical Review **77**, (1950): 370.
16. M. I. Eides, H. Grotsh, and V. A. Shelyuto, Theory of light hydrogen atoms, Physics Reports **342** (2001): 63–261.
17. W. R. Johnson, and G. Soff, The Lamb shift in hydrogen-like atoms, $1 \leq Z \leq 110$, Atomic Data and Nuclear Data **33** (1985): 405–446.
18. A. E. Kramida, A critical compilation of experimental data on spectral lines and energy levels of hydrogen, deuterium, and tritium, Atomic Data and Nuclear Tables **96**, 6 (2010).
19. B. H. Bransden, and C. J. Joachain, Physics of Atoms and Molecules (Pearson, 2003), Eq. (5.157).
20. M. Horbatsch, and E. A. Hessels, Tabulation of the bound-state energies of atomic hydrogen, Physical Review A **93**, 022513 (2016), Tables III, IV, V.
21. B. R. Clarke, Reinterpretation of the Grangier experiment using a multiple-triggering single-photon model, Modern Physics Letters B **37**, 15, 2350042 (2023).
22. U. Jentschura, and V. A. Yerokin, Physical Review A, **73**, 062503 (2006).
23. S. G. Karshenboim, Precision physics of simple atoms: QED tests, nuclear structure and fundamental constants, Physics Reports, 422, 1–2 (2005): 1–63.
24. E. Tiesinga, P. J. Mohr, D. B. Newell, and B. N. Taylor, CODATA recommended values of the fundamental physical constants: 2018, Reviews of Modern Physics **93** (April–June 2021), Tables XXX and XXXI.